The Relationship between Anticyclonic Anomalies in Northeast Asia and Severe Haze in the Beijing-Tianjin-Hebei Region

Wogu Zhong [1,2], Zhicong Yin [1,2*] and Huijun Wang [1,2]

[1]Key Laboratory of Meteorological Disaster, Ministry of Education / Joint International Research Laboratory of Climate and Environment Change (ILCEC) / Collaborative Innovation Center on Forecast and Evaluation of Meteorological Disasters (CIC-FEMD), Nanjing University of Information Science & Technology, Nanjing 210044, China

[2]Nansen-Zhu International Research Centre, Institute of Atmospheric Physics, Chinese Academy of Sciences, Beijing, China

[*]*Correspondence to*: Zhicong Yin (yinzhc@163.com)

Abstract. Haze pollution in the Beijing-Tianjin-Hebei (BTH) region has become increasingly more severe and persistent in recent years. To better understand the formation of severe haze and its relationship with anticyclonic anomalies over Northeast Asia (AANA), this research focused on severe haze over the BTH region occurring in December during 2014-2016 and examined the impacts of the AANA. The results indicated that local meteorological conditions were conducive to severe haze (such as weaker surface winds, a stronger temperature inversion, a shallower boundary layer, and higher relative humidity) and were all closely related to the AANA. During severe haze episodes, the AANA remained strong in the mid-upper troposphere, generating anomalous southeasterly winds near the surface. This effect not only promoted the accumulation of pollutants due to the unique topographical conditions in the BTH region, but also caused warm advection in lower levels, which was the main cause of the formation and development of temperature inversion layer. As a synoptic-scale circulation, the AANA was accompanied by anomalous vertical motions in the surrounding areas, which weakened the meridional circulation over the BTH region. The intrusions of the clean air from upper levels to the surface and the downward transportation of westerly momentum were suppressed, resulting in weaker northerly winds near the surface and a shallower boundary layer. The thermally indirect zonal circulation between the BTH region and western Pacific triggered by the AANA provided a persistent source of moisture to the BTH region, which strengthened the development of severe haze by promoting the growth of fine particles. The advance and retreat of the AANA often corresponded with the emergence and dissipation of severe haze, illustrating that the AANA could be an effective forecast indicator for air quality.

Key words: severe haze pollution; $PM_{2.5}$; anticyclonic anomalies; air quality

1. Introduction

Haze is a weather phenomenon, which could restrict the visual range and increase the risk of traffic accidents; and haze is also a type of serious air pollution that is detrimental to people's health (Hu et al., 2015; Wang et al., 2016). Haze events in China are mainly caused by the fine particulate matter (PM), which contains primary pollutants and sulfate or nitrate aerosols (Wang et al., 2016; Cai et al., 2017; Shen et al., 2018). In recent years, the Beijing–Tianjin–Hebei (BTH, located at 36°-42°N, 114°-120°E) region has witnessed several severe haze events with long duration, large spatial extent and serious pollution levels. Notably, the number of haze days in the BTH region has increased, and the affected area has shown an interdecadal expanding trend (Zhang et al., 2015). To control the air pollution, the Chinese government promulgated the Air Pollution Prevention and Control Action Plan in 2013. So far, the atmospheric environment quality in the BTH region has improved to a certain extent, mainly via the reduction in SO_2 and NO_2 concentrations ("Formation Mechanism and Control Strategies of Haze in China" professional group, 2015). However, the decline in $PM_{2.5}$ concentration was not obvious, and the occurrence of severe haze events in the BTH region showed strong inter-annual variations, especially in the winter (Chen and Wang, 2015; Yin and Wang, 2018). Previous studies have revealed that the strong inter-annual variation of December haze days is different from that in other winter months (Yin and Wang, 2018). During 16-21 December 2016, the BTH region suffered serious air pollution. Despite more than 30 cities initiating an air pollution red alert ahead of time, the pollution lasted for five days, and the instantaneous $PM_{2.5}$ concentration reached up to 1000 $\mu g \cdot m^{-3}$ in Shijiazhuang, the capital of Hebei province. Another pollution event occurred from 30 December 2016 to 7 January 2017, lasting for as long as nine days. These two long-term severe haze pollution processes were detected within 20 days, which triggered a broader discussion over their formation, scientific attribution and reasonable methods of management (Wang, 2018).

Previous studies have indicated that the formation of severe haze is characterized by a complex interplay between anthropogenic emissions, chemical processes and meteorological factors (Wang et al., 2016; Tang et al., 2018). The basic cause of haze pollution is excessive emission (Wang et al., 2013; Zhang et al., 2013). The synergistic effects of these anthropogenic emissions may worsen air pollution in North China (Wang et al., 2016; Yang et al., 2016). Nevertheless, meteorological conditions still play a key role in the formation of haze events (Zhang et al., 2014; Yin and Wang, 2017a; Wei et al., 2017). According to recent research (Cai et al., 2017), atmospheric circulation changes induced by global warming may enhance the stability of the lower atmosphere in Beijing, leading to more frequent and severe haze pollution in the future. Furthermore, the decline of autumn Arctic sea ice and the negative anomalies of subtropical western Pacific sea surface temperature could greatly change the atmospheric circulation and lead to an increase in haze days in eastern China (Wang et al., 2015; Yin and Wang, 2016). Haze pollution could be exacerbated under these preceding force factors through their impacts on atmospheric circulations and meteorological conditions. In addition, local meteorological conditions and the structure of boundary layer will vary with the change in the large-scale circulation conditions, which could affect the dispersion capability of atmosphere

and thus have an effect on air pollution (Wu et al., 2017). The weather conditions affecting pollutant dispersion include dynamic factors (e.g., wind and turbulence) and thermodynamic factors (e.g., atmospheric stratification and its stability) (Zhang et al., 2014). Lower wind speed, higher relative humidity and stable atmospheric stratification are the main factors that are conducive to the occurrence of haze (Zhang et al., 2014; Ding and Liu, 2014; Yin et al., 2015b). Such weather conditions could be strengthened by a weaker East Asian winter monsoon (EAWM) and the positive phase of the East Atlantic-West Russia (EA/WR) teleconnection (Yin et al., 2015a; Wu et al., 2016; Yin and Wang, 2016).

Research on persistent and severe haze pollution in the BTH region has demonstrated that anticyclonic anomalies in Northeast Asia (AANA) represent a key local circulation that is conducive to the formation of serious haze pollution. Some studies have indicated that weak East Asian winter monsoon could modulate the AANA (Li et al. 2015; Yin et al. 2015a). With the decline of EAWM, cold air is restricted to high-latitude areas, and the East Asian trough becomes weak. It is physically reasonable that the weaker East Asian trough appears as anticyclonic circulations in the anomaly field. Thus, to some extent, the AANA is a representative indicator of EAWM systems (Wang and Jiang, 2004). However, it is still unclear how such atmospheric anomalies affect the severe haze events. To better represent the intensity of the AANA and its physical mechanism on haze pollution, we defined $AANAI_{Z500}$ ($AANAI_{\omega 500}$) and $AANAI_{V850}$ according to the composite anomalies at 500 hPa geopotential (vertical velocity) field and 850 hPa wind field on severe haze episodes, referring to previous EAWM indexes (Wang and Jiang, 2004; He and Wang, 2012). Considering that the air quality measurement network in China is relatively recently developed, this study focused on severe haze pollution in the BTH region during the months of December in the years 2014-2016, and explicated the characteristics of the AANA and its relationship with severe haze, while making comparison with non-haze episodes. The situation in December 2017 were also discussed to verify the relationship revealed in this study.

2. Data and method

Meteorological observation data at three-hour intervals in the months of December in the years 2014-2016 were obtained from China Meteorological Administration, including visibility, surface wind speed and surface relative humidity (RH). Hourly $PM_{2.5}$ concentration data from 80 national air quality stations over the BTH region were derived from the website of Ministry of Ecology and Environment of China. Additionally, the geopotential height at 500 hPa, sea level pressure (SLP), U and V components of wind at 200 hPa, 850 hPa and the surface, vertical velocity (omega) from 200 hPa to 1000 hPa, temperature at 850 hPa, 1000 hPa and the surface, surface dew point temperature, RH from 200 hPa to 1000 hPa, and planetary boundary layer height (PBLH) from the ERA-Interim reanalysis data (Dee et al., 2011) were downloaded from the European Centre for Medium-Range Weather Forecasts (ECMWF), with a horizontal resolution of 0.75°×0.75°. The distribution data of surface RH were calculated by the surface temperature and dew point temperature from the ERA-Interim reanalysis data. Considering that ERA-Interim might have problems capturing the day-to-day and diurnal variations of PBLH over North China (von Engeln

and Teixeira, 2013; Guo et al, 2016), the NCEP GDAS/FNL Global Surface Flux data were applied to make a comparison. The anomaly fields were calculated with respect to the mean climatology in December from 1979 to 2010. Considering of the strong diurnal variations of some meteorological factors, such as the PBLH, temperature and RH, the climatology here were calculated separately for 02:00, 08:00, 14:00 and 20:00 in Beijing local time.

Considering that national air quality stations over the BTH region are scarce and unevenly distributed, here we made up Thiessen polygons to calculate the weighted average of $PM_{2.5}$ concentration and built time series at intervals of six hours. Then, we selected the severe haze events (defined as $PM_{2.5}$ concentration $\geq 150\ \mu g \cdot m^{-3}$; Cai et al., 2017) and non-haze events ($PM_{2.5}$ concentration $\leq 50\ \mu g \cdot m^{-3}$) and used composite analysis to analyze the associated atmospheric circulations and weather conditions. Most previous studies investigated haze events in units of hours or days and the variations among haze pollution processes were not taken into account. Some meteorological factors might be closely related to haze pollution in a few cases but remain insignificant in others. In this way, the relationship between haze pollution and meteorological factors might be overemphasized. Meanwhile, some meteorological factors, such as the PBLH and RH, showed strong temporal variations, which might call their statistical relationship with haze pollution into question. Thus, neglecting the small time-scale disturbances within each synoptic-scale environment could help to obtain the physical insight (Lackmann, 2011). To better describe the relationships and mechanisms manifesting among different haze pollution processes, new data called synoptic process mean (SPM) data were rebuilt. According to the $PM_{2.5}$ concentration, the synoptic-scale environments were divided into three groups: severe haze, non-haze and non-severe haze (i.e., $PM_{2.5}$ concentration $\subseteq [50,150]\ \mu g \cdot m^{-3}$). Two criteria were used to ensure each type of haze pollution process was typical and mutual independent: (1) a haze pollution process should have a minimum duration for at least 12 hours (i.e., two timesteps; a timestep represents 6 hours); (2) if any two haze pollution processes of the same type were detected within 24 hours (i.e., four timesteps), these two processes would be merged into one. The SPM data applied time averaging method to calculate the mean $PM_{2.5}$ concentration and all the meteorological data during each haze pollution process. Based on the SPM data, the synoptic process correlation coefficients (SPCCs) were calculated in the units of haze pollution processes, rather than in units of hours or days. This method maintains the physical relations between haze and meteorological factors while removing the potential influence of the day-to-day and diurnal variations inside each synoptic-scale environment. In addition, the vertical transport of westerly momentum was defined as $\frac{\partial u\omega}{\partial P}$ in this study (Zhong et al., 2010). $\frac{\partial u\omega}{\partial P} < 0$ represents the downward transport of westerly momentum, and $\frac{\partial u\omega}{\partial P} > 0$ represents the upward transport of westerly momentum (i.e., the downward transport was restricted).

3. Results

Figure 1 shows the six-hour variation of $PM_{2.5}$ concentration over the BTH region in December 2014, December 2015 and December 2016. The monthly mean concentrations in 2014-2016 were 84.7 $\mu g \cdot m^{-3}$, 126.4 $\mu g \cdot m^{-3}$, and

128.1 $\mu g \cdot m^{-3}$, and the standard deviations were 55.4 $\mu g \cdot m^{-3}$, 79.1 $\mu g \cdot m^{-3}$, and 70.9 $\mu g \cdot m^{-3}$, respectively. These results demonstrated that haze pollution in December was serious and fluctuated strongly. The first and third quartiles of the series were 54.0 $\mu g \cdot m^{-3}$ and 156.7 $\mu g \cdot m^{-3}$, indicating that the threshold values of severe haze (150 $\mu g \cdot m^{-3}$) and non-haze (50 $\mu g \cdot m^{-3}$) events were reasonable. There were 14 severe haze and 12 non-haze events in the months of December in the years 2014-2016 (Table 1). The duration time of severe haze events (9.3 timesteps) was relatively longer than that of non-haze events (8.9 timesteps), especially in 2015 and 2016. Severe haze broke out rapidly in most cases, but the dissipation processes varied in different years. The $PM_{2.5}$ concentration decreased relatively quickly in 2014, while it remained at high concentration levels before decreasing in 2015 and 2016. Specific to the severe haze since 15 December 2016, most cities in the BTH region and the surrounding areas issued an air pollution red alert ahead of time, and anthropogenic discharges were strictly controlled. Despite those efforts, the BTH region was still hit by serious and persistent haze, demonstrating that meteorological conditions had a significant impact on haze pollution (Yin and Wang, 2017b).

As a critical system influencing the climate pattern over East Asia, EAWM plays an important role in the formation of severe haze (Zhang et al., 2014; Yin et al., 2015; Yin and Wang, 2017b). When severe haze occurred, the EAWM weakened from the upper to the lower troposphere, which could be verified by the relatively weak geopotential height patterns over the Siberia and the Aleutian Islands at mid-levels (Figure 2a), the decline in northerly winds near the surface (Figure 3a–b) and warmer land surface (Figure 2b). As a consequence, the East Asian jet stream was weaker and moved northward with respect to the climatological mean (Yin and Wang, 2017b), while the East Asian trough declined and moved eastwards (Figure 2a). These results indicated that the meridional circulation over the middle-high latitude area in East Asia was weakened and that the BTH region was mainly occupied by zonal circulation. Thus, cold air intrusions were suppressed, and their southward movement into the BTH region decreased (Chen and Wang, 2015; Yin and Wang, 2017b). The negative anomalies of the SLP were obvious over the middle-high latitude area in the Eurasian continent, with two negative centers located over the Siberian plain and Bering Strait, while the SLP anomaly in the Western Pacific was positive (Figure 2b). The change in differences between land and sea induced southeasterly winds. Considering that the BTH region is located in the southeast of the Taihang-Yanshan mountains, wind anomalies could restrict the dispersion of pollutants. Moreover, the warm air brought by southeasterly winds strengthened the intensity of temperature inversion potential (TIP, T_{850}-T_{1000}). The emergence of stable stratification restricted the vertical dispersion of pollutants (Figure 3a). When it came to non-haze events, the EAWM was relatively strong in the troposphere (Figure 2c–d). Thus, the cold air incursions became more frequent, resulting in stronger surface winds and lower surface RH in the BTH region (Figure 3c–d). In addition, the pressure differences between the Western Pacific and BTH region increased relatively, and the northerly winds were strengthened, accelerating the decrease in the $PM_{2.5}$ concentration. In general, the weakening of the EAWM restricted the cold air invasions and had an impact on local weather conditions, including surface wind speeds, surface RH and TIP, whose SPCCs with the mean $PM_{2.5}$ concentration in the BTH

region were -0.42, 0.72 and 0.56, respectively, and all exceeded the 99% confidence level (Table 2). With the decline in the wind speed near the surface and the increase in the TIP, the horizontal and vertical dispersion of the pollutants were inhibited, while higher surface RH exacerbated the formation of contaminants. These factors led to a rapid increase in the $PM_{2.5}$ concentration and resulted in severe haze (Figure 4).

The aforementioned southeasterly wind, abundant moisture and strong temperature inversion that induced severe haze were all closely related to the AANA (Figure 4–5). Thus, we evaluated the AANA as a key circulation pattern influencing severe haze in the BTH region. Here, we defined three indexes: $AANAI_{Z500}$ (defined as Z_{500} anomalies over 115-140°E, 30-50°N, i.e., in the white box in Figure 2a), $AANAI_{V850}$ (defined as wind speed anomalies at 850 hPa over 120-150°E, 30-40°N, i.e., in the black box in Figure 3a) and $AANAI_{\omega 500}$ (defined as $\boldsymbol{\omega}_{500}$ anomalies over 115-125°E, 35-45°N, i.e., in the white box in Figure 6a) to describe the intensity of the AANA in the mid and lower troposphere. Note that the $AANAI_{Z500}$ and $AANAI_{V850}$ were similar to previous EAWM indexes (Wang and Jiang, 2004; He and Wang, 2012), since the AANA was an important manifestation of the weaker EAWM (Figure 2a). However, here we defined these indexes through anomaly fields to analyze anomalous atmospheric circulations, differing from the EAWM indexes, which were used to describe the intensity of the EAWM and its climatic evolution. The physical meaning and the critical areas taking into account were different between the $AANAI_{Z500}$ ($AANAI_{V850}$) and EAWM indexes. Considering that the $AANAI_{Z500}$ and $AANAI_{V850}$ only represented the intensity of the AANA in the horizontal dimension, we further introduced $AANAI_{\omega 500}$ to investigate the vertical structure of the AANA. This part will be illustrated in detail in the following section. We calculated the SPCC between the mean $PM_{2.5}$ concentration in the BTH region and the $AANAI_{Z500}$ ($AANAI_{V850}$), and it was 0.64 (-0.64), exceeding the 99% confidence level (Table 2). Thus, the AANA was closely related to the emergence and development of haze pollution (Figure 5). When severe haze took place, the AANA could be identified from the lower to the upper levels, especially at mid-troposphere (Figure 6a). The AANA could generate southeasterly winds near the surface (Figure 3a), which was encouraged to the accumulation of pollutants and water vapor. Southeasterly winds gathered pollutants from the surrounding areas and provided a steady supply of fine particles for haze pollution in the BTH region, while bringing moisture from the Western Pacific to the BTH region via Bohai Bay. With the weak convergence induced by the anomalous low surface pressure, moisture was transported to the BTH region (Figure 3b). This promoted the hygroscopic growth of fine particles and the formation of secondary pollutants (Wang et al, 2016). In addition, the warm advection over the BTH region induced by southeasterly winds could be verified in the middle and lower troposphere (Figure 7). Strong warm advection at mid-levels was also consistent with the decline in the EAWM. Specifically, the local temperature changes mainly generated by warm advection were stronger at 850 hPa than those at 1000 hPa at the day before the first day of severe haze events. Even though anomalous vertical motions had negative effects on the change of temperature at the first day of severe haze events, the positive horizontal advection still prevailed in lower levels and the local temperature changes remained positive (Figure 7). These effects were propitious to the formation and development of

temperature inversion layer and the increase in atmospheric stability (Figure 3a). The SPCC between the $AANAI_{Z500}$ and TIP was 0.58 and exceeded the 95% confidence level (Table 3). For non-haze events, Northeast Asia was mainly controlled by cyclonic anomalies (Figure 6b), which strengthened northerly winds near the surface (Figure 3c). Strong northerly winds brought about cold advection over the BTH region and restrained the transport of water vapor (Figure 3d). Higher wind speeds and a drier atmosphere were conducive to the dispersion of pollutants. The SPCC between the $AANAI_{Z500}$ and surface wind speed (surface RH) was -0.38 (0.73), exceeding the 99% confidence level (Table 3). Thus, because of the unique topographical conditions in the BTH region, the anomalous southeasterly flows caused by the AANA facilitated the formation and aggregation of haze particles. The emergence of temperature inversion layer enhanced the atmospheric stability, leading to more persistent and serious haze events. Aside from horizontal dispersion, vertical dispersion also played a vital role in haze pollution (Zhao et al, 2013; Wu et al, 2017). When severe haze occurred, the negative anomalies of vertical velocity (omega) were focused over Northeast Asia and coastal regions of eastern China, while positive anomalies were mainly located in Northwestern Pacific (Figure 6a). Thus, the mid-level reflection of AANA was accompanied by anomalous synoptic-scale ascending (descending) motions to the rear (front) of the AANA. The distribution of anomalies was opposite in non-haze events: cyclonic anomalies appeared with anomalous synoptic-scale ascending (descending) motions to the front (rear) of cyclonic anomalies (Figure 6b). In particular, the SPCC between the $AANAI_{\omega 500}$ and the mean $PM_{2.5}$ concentration in the BTH region was -0.70, exceeding the 99% confidence level (Table 2). This result demonstrated that the anomalous synoptic-scale ascending motions to the rear of the AANA had a significant effect on haze pollution in the BTH region. Our results appeared to contradict with the insufficient speculation by Yin and Wang (2017b), which simply concluded the sinking motion generated by the AANA as the overall state. The following sections explain how the associated vertical circulation affected severe haze in the BTH region.

The anomalous synoptic-scale ascending motion associated with the AANA extended through the depth of the troposphere (Figure 8). Considering of the climate mean state over the BTH region (i.e., descending motion; Figure S1), the anomalous ascending flow weakened the vertical motion in the local area when severe haze occurred, and even generated weak ascending motions in the lower troposphere (i.e., 500-800 hPa; Figure 9a). Even though sinking motions still prevailed over the BTH region, the sink of cold air from upper levels was greatly weakened due to the anomalous ascending flow (Figure 9a). This effect might explain why the subsidence and associated adiabatic warming weakened during severe haze episodes and did not predominate in the changes of lower level temperature (Figure 7). The strong warm advection mentioned above (Figure 7) represented the decline in the dry air intrusion (Sun et al., 2017). As a result, the invasion of cold and dry air from upper levels to the surface was relatively weak, which provided favorable conditions for the formation of severe haze (Sun et al., 2017; Hu et al., 2018). The anomalous ascending motion in the middle troposphere not only weakened the normal sinking flow, but also confined the downward transportation of westerly momentum (i.e., $\frac{\partial u\omega}{\partial P}>0$, Figure 9b), which led to weaker northerly winds

near the surface (Lu et al., 2010; Liu and Guo, 2012). The inhibited downward momentum was the reflection of a less frequent cold air intrusion (Hu et al., 2018), and it could also affect the intensity of turbulence. On one hand, with the weakening of momentum exchange between the upper and lower levels, the transformation of kinetic energy from the basic flow to the turbulent flow was restrained (Liu et al., 2011). On the other hand, the temperature inversion mainly generated by anomalous southeasterly winds would lead to the increase in atmospheric stability and dissipate the turbulent kinetic energy. In this situation, the kinetic energy of turbulence decreased (Liu et al., 2011). Weaker turbulence could be verified by a shallower planetary boundary layer (Figure 3a). The PBLH over the BTH region was only 266.7m during severe haze episodes (the mean state of PBLH in December is 430.7m according to the ERA-interim data). This reduced the atmosphere's capacity for pollution aerosols and had adverse effects on the dispersion of pollutants. The SPCC between the PBLH anomalies and the $PM_{2.5}$ concentration was -0.60, passing the 99% confidence level (Table 2). It is worth noting that the emergence of inversion layer in the BTH region resulted in a more stable atmosphere, and thus the aforementioned anomalous ascending flow could not connect with the air that lying beneath the stable layer (Corfidi et al. 2008). However, the anomalous vertical flow still provided favorable synoptic-scale environments by confining the clean air intrusion and the downward momentum from upper levels. Once anomalous ascending flows weakened and descending motions prevailed over the BTH region, the sink of clean air from upper levels tended to break the inversion layer (Figure 7c). This effect could also strengthen the downward momentum and northerly winds near the surface. Subsequently, the BTH region was mainly controlled by the cold advection (Figure 7c). These factors represented the dissipation process for haze pollution. For the non-haze episodes, the cyclonic circulation induced anomalous descending motions over the BTH region, which strengthened the local meridional circulation (Figure 8c–d) and the downward transport of westerly momentum (Figure 9c–d). Under these circumstances, the clean air intrusion from free troposphere was more frequent, and the surface wind speeds and turbulent exchange were enhanced, leading to conducive conditions for pollutant dispersion. In general, the AANA was accompanied by anomalous synoptic-scale ascending flows to its rear, which weakened the normal meridional circulation over the BTH region and the clean air intrusions from higher levels. The resulting weak local vertical circulation also restrained the transportation of downward momentum and led to the conditions of lower surface wind speeds, weaker turbulence and a shallower boundary layer in the local area. These effects provided favorable synoptic-scale environments for the formation and development of severe haze.

Note that the AANA modulated a thermally indirect zonal circulation between the BTH region and Western Pacific (i.e., ascending motions over the land and descending motions over the sea; the mean state over this region in the boreal winter is ascending motions over the relatively warm sea and descending motions over the relatively cold land, see Figure. S2), which acted as an important water vapor path (Figure 8b). The easterly winds in the lower troposphere triggered by the AANA brought humid and warm air to the BTH region and resulted in higher RH in the lower (900-1000 hPa) atmosphere. This effect could accelerate the growth of fine particles and lead to a sharp increase in $PM_{2.5}$ concentration. Higher RH near the surface also

restrained evaporation, which restricted the development of turbulence (Betts, 1997). Consequently, the anomalous ascent was weak near the surface relative to the anomalies in the lower and middle troposphere. Weak updrafts near the surface could not make the pollutants disperse in the vertical direction (Sun et al., 2017; Yin and Wang, 2018). Moreover, the aforementioned temperature inversion layer could lead to weaker turbulence, which discouraged the ascending motion in lower levels from connecting with the air in upper levels. During non-haze events, the thermally direct vertical circulation (i.e., ascending motions over the sea and descending motions over the land) could be verified beneath the control area of the AANA, through which pollutants and water vapor were transported to the ocean. The resulting drier atmosphere over the BTH region restrained the growth of fine particles. In brief, the thermally indirect circulation between land and sea modulated by the AANA provided a persistent source of water vapor for severe haze, and the resulting higher RH weakened the turbulence. These effects might explain why severe haze tended to last for a long time.

We further investigated the evolution processes of the AANA on severe haze/non-haze episodes to provide a basis for air quality forecasting. Before severe haze episodes, Northeast Asia was mainly occupied by cyclonic circulation, which had the tendency of weakening over time (Figure 10a–c). This effect was caused by the strengthening of positive anomalies over Lake Baikal. The eastward propagation of positive anomalies over Lake Baikal was a precursory signal of severe haze. On the first day of severe haze, the AANA was relatively typical and strong at the mid-level, with anomalous ascending motions over the BTH region and anomalous southeasterly winds near the surface (Figure 10d). These anomalies regulated the synoptic-scale environments and provided favorable conditions for the formation of severe haze. The AANA moved to the east continually after the first day of severe haze (Figure 10e-f). Three days after severe haze, the AANA was replaced by a cyclonic circulation and haze pollution tended to dissipate (Figure 10g). The rebuilding of a cyclonic circulation over the BTH region represented the end of severe haze. For the non-haze episodes, the AANA remained strong and moved slowly before the non-haze day (Figure 10h-j). Few cyclones developed, which were mainly located in the high-latitude area. The switch from an anticyclonic circulation to a cyclonic system occurred a day before the non-haze day, which was associated with polar cold air entering into the BTH region. On the first non-haze day, a cyclonic circulation developed over Northeast Asia (Figure 10k). The anomalous descending motion over the BTH region and the northerly wind near the surface could be verified. One day after the non-haze day, the anomalous descending motions were enhanced with the development of the cyclonic circulation (Figure 10l). Subsequently, the cyclonic circulation moved eastward by the positive anomaly over Lake Baikal (Figure 10n). In brief, the emergence and development of severe haze (non-haze) was matched by the movements of the AANA. Thus, the AANA could be an effective forecast indicator for air quality.

4. Conclusions and discussions

Severe haze in the BTH region has become more serious and persistent in recent years, which has wreaked havoc on

society and economy. Basing on the $PM_{2.5}$ concentration data collected from the air quality measurement network in China, this research focused on severe haze episodes over the BTH region during the months of December in the years 2014-2016. Non-haze episodes were also taken into account as a comparison. The associated atmospheric circulations and the structure of the AANA were analyzed. The results indicated that the AANA was closely related to weaker surface winds, a stronger temperature inversion, a shallower boundary layer, and higher RH in the BTH region, which were of importance in the formation of severe haze. The AANA motivated southeasterly winds in the lower troposphere, gathering pollutants and moisture to the BTH region. Strong southeasterly winds also generated temperature inversion through warm advection, which strengthened the stability of lower atmosphere. As a synoptic-scale system, the AANA was accompanied by anomalous vertical motions in the surrounding areas. This weakened the local meridional circulation and the invasions of cold and dry air from higher levels. Meanwhile, the anomalous vertical motion restrained the downward transport of momentum and resulted in lower surface wind speeds, weaker turbulence and a shallower boundary layer, which were highly detrimental to pollutant dispersion. The AANA also modulated a thermally indirect circulation between land and sea, which acted as the main moisture path. Abundant moisture promoted the growth of haze particles, and higher RH weakened turbulence. These factors provided favorable conditions for the emergence and development of severe haze. The evolution processes of the AANA on severe haze/non-haze episodes were also discussed. The positive anomalies in Lake Baikal stretched eastward continuously before the AANA occupied Northeast Asia, which was a precursory signal of severe haze. In contrast, a transition from anticyclonic circulation to cyclonic circulation occurred a day before the non-haze day, resulting in the rapid movement of polar cold air.

It is well acknowledged that the fine PM is the main cause of severe haze in China (Wang et al., 2016; Cai et al., 2017). Compared with visibility used in previous researches (Chen and Wang, 2015; Yin et al., 2015a; Yin et al., 2015b), the $PM_{2.5}$ concentration could represent the characteristics of haze pollution better. Thus, the severe and non-haze events analyzed in this research were sorted out according to $PM_{2.5}$ concentration, while the visibility data were included to draw a comparison with previous researches. The basic results that stronger AANA, corresponding to a weaker EAWM, could lead to severe haze by generating weaker surface winds, a stronger temperature inversion and higher RH were in agreement with previous findings (Yin et al., 2015a; Yin and Wang, 2017b). Strong correlations between AANA indexes and visibility also existed (Table 3 and table 5). In addition, this study offered novel insights into the formation of severe haze in the BTH region. Our analysis demonstrated the dynamic mechanism of how the AANA affected severe haze in the BTH region. The AANA not only motivated southeasterly winds near the surface but also modulated anomalous vertical motions. These synoptic-scale environments led to conducive local meteorological conditions for severe haze, including weaker surface winds, a stronger temperature inversion, a shallower boundary layer and higher RH. The situation in December 2017 backed up our conclusions. Even though the haze events were not as serious as those in previous years, the AANA could be detected at the mid-level when severe haze occurred (Figure 11a). BTH region was occupied by anomalous southerly winds near the surface and anomalous

ascending motions in upper levels. The strong cyclonic circulation over Northeast Asia might explain why the haze pollution was less severe in December 2017 (Figure 11b). In the different years, the relationship between the AANA and severe haze in the BTH region expressed different features but remained strong. In 2014, 2016 and 2017, the SPCCs between the $PM_{2.5}$ concentration and $AANAI_{Z500}$ were 0.81, 0.79 and 0.73, respectively, all passing the 99% confidence level (Table 4). These results indicated that the AANA could play an important role in the formation of severe haze over the BTH region in 2014, 2016 and 2017. However, the SPCC between the $PM_{2.5}$ concentration and the $AANAI_{Z500}$ was 0.53 in 2015, and it failed to pass the confidence test. It might be associated with the influence of ENSO on the mid-tropospheric circulation. Although the AANA was not evident in the mid-level, it still emerged in the lower troposphere and had an impact on severe haze. The SPCC between the $PM_{2.5}$ concentration and $AANAI_{v850}$ ($AANAI_{\omega 500}$) was -0.61 (-0.66), exceeding the 95% confidence level (Table 4). In addition, there were some differences on how the AANA affected severe haze. In 2014, the AANA strengthened the severe haze mainly by enhancing TIP anomalies and surface RH, whose SPCC with the $AANAI_{Z500}$ were 0.62 and 0.57, respectively (Table 5). The AANA could promoted weaker surface winds, higher surface RH and a shallower boundary layer in 2015. The SPCCs between the AANAI $_{v850}$ and surface wind speed, surface RH and ERA PBLH anomalies were 0.74 -0.70 and 0.64, respectively (Table 5). Similar situation could be detected in 2016 and 2017 (Table 5). These results proved that the AANA indexes could capture the relationship between severe haze in the BTH region and the synoptic-scale environments. It is worth noting that the tendency for ERA-Interim to underestimate PBLH (von Engeln and Teixeira, 2013) may be less of an issue during winter over North China (Guo et al, 2016). We have further calculated the SPCCs between AANA indexes and FNL PBLH (Table 5), which confirmed that our conclusions are not dependent on the reanalysis dataset. Higher RH over the BTH region could be verified in upper levels (200-300 hPa; Figure 8b) because evaporated water vapor over the ocean could be transported to the air over the land by anomalous easterly flows. Further research remains necessary to explore how higher RH in upper levels affects severe haze. The evolution processes of the AANA on severe haze/non-haze episodes illustrated that the intensity of the AANA could play an important role in the emergence and dissipation of severe haze. However, the severe haze/non-haze events analyzed in this study were limited to the months of December in the years 2014-2016. Further analysis containing more sample data is required to confirm whether the three AANA indexes we defined in this study could be reliable forecast indicators.

Acknowledgements:

This research was supported by the National Key Research and Development Plan (2016YFA0600703), the National Natural Science Foundation of China (41705058 and 91744311), the funding of Jiangsu innovation & entrepreneurship team, 2017 Jiangsu Province College Students Innovation and Entrepreneurship Training Program (201710300007), and the Priority Academic Program Development (PAPD) of Jiangsu Higher Education Institutions.

References

Betts, A. K.: The Parameterization of Deep Convection. The Physics and Parameterization of Moist Atmospheric Convection. Springer, Netherlands, 255-279, 1997.

Cai, W. J., Li, K., Liao, H., et al.: Weather conditions conducive to Beijing severe haze more frequent under climate change. *Nature Climate Change*, **7**, 257–262, doi:10.1038/nclimate3249, 2017.

Chen, H. P. and Wang, H. J.: Haze Days in North China and the associated atmospheric circulations based on daily visibility data from 1960 to 2012. *J. Geophys. Res.*, **120**, 5895-5909, doi:10.1002/2015JD023225, 2015.

Corfidi, S. F., Corfidi, S. J., and Schultz, D. M.: Elevated Convection and Castellanus: Ambiguities, Significance, and Questions. *Wea. Forecasting*, **23**, 1280-1303, doi:10.1175/2008WAF2222118.1, 2008.

Dee D. P., Uppala S. M., Simmons A. J., et al.: The ERA-Interim reanalysis: configuration and performance of the data assimilation system. *Q. J. Roy. Meteor. Soc.*, **137**, 553–597, doi:10.1002/qj.828, 2011.

Ding, Y. H. and Liu, Y. J.: Analysis of long-term variations of fog and haze in China in recent 50 years and their relations with atmospheric humidity. *SCIENCE CHINA Earth Sciences*, **57**, 36-46, doi:10.1007/s11430-013-4792-1, 2014.

"Formation Mechanism and Control Strategies of Haze in China" professional group.: Assessment report on PM_(2.5) control effects in the Beijing-Tianjin-Hebei region since the implement of Air Pollution Prevention and Control Action Plan. *Bulletin of Chinese Academy of Sciences*, **30**, 668-678, doi:10.16418/j.issn.1000-3045.2015.05.012, 2015.

Guo, J. P., Miao, Y. C., Zhang, Y., et al.: The climatology of planetary boundary layer height in China derived from radiosonde and reanalysis data, *Atmos. Chem. Phys.*, **16**, 13309-13319, doi:10.5194/acp-16-13309-2016, 2016.

He, S. P. and Wang, H. J.: An Integrated East Asian Winter Monsoon Index and Its Interannual Variability. *Chinese Journal of Atmospheric Sciences*, **36**, 523-538, doi:10.3878/j.issn.1006-9895.2011.11083, 2012.

Hu, B., Chen, R., Xu, J. X., et al.: Health effects of ambient ultrafine (nano) particles in haze. *Chinese Science Bulletin*, **60**, 2808-2823, doi:10.1360/N972014-01404, 2015.

Hu, Y. L., Wang, S. G., Ning, G. C., et al.: A quantitative assessment of the air pollution purification effect of a super strong cold-air outbreak in January 2016 in China. *Air Qual. Atmos. Health.*, **11**, 907-923, doi:10.1007/s11869-018-0592-2, 2018.

Lackmann, G.: Midlatitude synoptic meteorology: dynamics, analysis, and forecasting, American Meteorological Society, Boston, America, 5-10, 2011.

Li, Q., Zhang, R. H., Wang, Y.: Interannual variation of the winter-time fog–haze days across central and eastern China and its relation with East Asian winter monsoon. *Int. J. Climatol.,* **36**, 346–354, doi:10.1002/joc.4350, 2015.

Liu, S. K. and Liu, S. D.: Atmospheric dynamics. 2nd ed., Peking University Press, Beijing, China, 143-147, 2011.

Liu, X. E. and Guo, X. L.: Role of Downward Momentum Transport in the Formation of Severe Surface Winds, *Atmospheric and Oceanic Science Letters*, **5**, 379-383, doi:10.1080/16742834.2012.11447020, 2012.

Lu, C. S., N, S. J., Yang, J., et al.: Jump Features and Causes of Macro and Microphysical Structures of a Winter Fog in Nanjing. *Chinese Journal of Atmospheric Sciences*, **34**, 681-690, doi:10.3878/j.issn.1006-9895.2010.04.02, 2010.

National Centers for Environmental Prediction/National Weather Service/NOAA/U.S. Department of Commerce.: NCEP GDAS/FNL 0.25 Degree Global Tropospheric Analyses and Forecast Grids. Research Data Archive at the National Center for Atmospheric Research, Computational and Information Systems Laboratory. https://doi.org/10.5065/D65Q4T4Z. Accessed 1 Jan 2019, 2015.

Shen, L., Jacob, D. J., Mickley, L. J., et al.: Insignificant effect of climate change on winter haze pollution in Beijing, *Atmos.*

Chem. Phys., **18**, 17489-17496, doi:10.5194/acp-18-17489-2018, 2018.

Sun, X. C., Han, Y. Q., Li, J., et al.: Analysis of the Influence of Vertical Movement on the Process of Fog and Haze with Air Pollution. *Plateau Meteorology*, **36**, 1106-1114, doi:10.7522/j.issn.1000-0534.2016.00076, 2017.

Tang, B. Y., Xin, J. Y., Gao, W. K., et al.: Characteristics of complex air pollution in typical cities of North China. *Atmospheric and Oceanic Science Letters*, **11**, 29-36, doi:10.1080/16742834.2018.1394158, 2018.

von Engeln, A. and Teixeira, J.: A planetary boundary layer height climatology derived from ECMWF reanalysis data. *J. Climate*, **26**, 6575–6590, doi:10.1175/JCLI-D-12-00385.1, 2013.

Wallace, J. M. and Hobbs, P. V.: Atmospheric science: an introductory survey. 2nd ed., Elsevier Academic Press, Amsterdam, 283, 2006.

Wang, H. J.: On assessing haze attribution and control measures in China. *Atmospheric and Oceanic Science Letters*, **11**, 120-122, doi:10.1080/16742834.2018.1409067, 2018.

Wang, H. J., Chen, H. P. and Liu, J. P.: Arctic sea ice decline intensified haze pollution in eastern China. *Atmospheric and Oceanic Science Letters*, **8**, 1-9, doi:10.3878/AOSL20140081, 2015.

Wang, H. J., Jiang, D. B.: A new East Asian winter monsoon intensity index and atmospheric circulation comparison between strong and weak composite. *Quaternary Sciences*, **24**, 19-27, doi:10.3321/j.issn:1001-7410.2004.01.003, 2004.

Wang, Y. S., Yao, L., Liu, Z. R., et al.: Formation of haze pollution in Beijing-Tianjin-Hebei region and their control strategies. *Bulletin of Chinese Academy of Sciences*, **28**, 353-363, doi:10.3969/j.issn.1000-3045.2013.03.009, 2013.

Wang, G. H., Zhang, R. Y., Gomez, M. E., et al.: Persistent sulfate formation from London Fog to Chinese haze. *Proceedings of the National Academy of Science*, **113**, 13630–13635, doi:10.1073/pnas.1616540113, 2016.

Wei, Y., Li, J., Wang, Z. F., et al.: Trends of surface PM2.5 over Beijing–Tianjin–Hebei in 2013–2015 and their causes: emission controls vs. meteorological conditions. *Atmospheric and Oceanic Science Letters*, **10**, 276-283, doi:10.1080/16742834.2017.1315631, 2017.

Wu, P., Ding, Y. H., Liu, Y. J., et al.: Influence of the East Asian winter monsoon and atmospheric humidity on the wintertime haze frequency over central-eastern China. *Acta Meteorologica Sinica*, **74**, 352-366, doi:10.11676/qxxb2016.029, 2016.

Wu, P., Ding, Y. H. and Liu. Y. J.: Atmospheric circulation and dynamic mechanism for persistent haze events in the Beijing–Tianjin–Hebei region. *Advances in Atmospheric Sciences*, **34**, 429–440, doi:10.1007/s00376-016-6158-z, 2017.

Yang, T., Sun, Y. L., Zhang, W., et al.: Chemical characterization of submicron particles during typical air pollution episodes in spring over Beijing. *Atmospheric and Oceanic Science Letters*, **9**, 255-262, doi:10.1080/16742834.2016.1173509, 2016.

Yin, Z. C., Wang, H. J. and Yuan, D. M.: Interdecadal increase of haze in winter over North China and the Huang-huai Area and the weakening of the East Asia Winter Monsoon. *Chinese Science Bulletin*, **60**, 1395-1400, doi:10.1360/N972014-01348, 2015a.

Yin, Z. C., Wang, H. J. and Guo, W. L.: Climatic change features of fog and haze in winter over North China and Huang-Huai Area. *SCIENCE CHINA Earth Sciences*, **58**, 1370-1376. doi:10.1007/s11430-015-5089-3, 2015b.

Yin, Z. C. and Wang, H. J.: The relationship between the subtropical Western Pacific SST and haze over North-Central North China Plain. *Int. J. Climatol.,* **36**, 3479-3491, doi:10.1002/joc.4570, 2016.

Yin, Z.C., Wang, H. J. and Chen, H. P.: Understanding severe winter haze events in the North China Plain in 2014: roles of climate anomalies. *Atmos. Chem. Phys.*, **17**, 1641-1651, doi:10.5194/acp-17-1641-2017, 2017a.

Yin Z. C. and Wang H. J.: Role of Atmospheric Circulations on Haze Pollution in December 2016. *Atmos. Chem. Phys.,* **17**,

11673-11681, doi:10.5194/acp-17-11673-2017, 2017b.

Yin Z. C. and Wang H. J.: The Strengthening Relationship between Eurasian Snow Cover and December Haze Days in Central North China after the Mid-1990s. *Atmos. Chem. Phys.*, **18**, 4753-4763, doi:10.5194/acp-18-4753-2018, 2018.

Zhao, X. J., Zhao, P. S., Xu, J., et al.: Analysis of a winter regional haze event and its formation mechanism in the North China Plain. *Atmos. Chem. Phys.*, **13**, 5685-5696, doi:10.5194/acp-13-5685-2013, 2013.

Zhang, X. Y., Sun, J. Y., Wang, Y. Q, et al.: Factors contributing to haze and fog in China. *Chinese Science Bulletin*, **58**, 1178-1187, doi:10.1360/972013-150, 2013.

Zhang, R. H., Li, Q. and Zhang, R. N.: Meteorological conditions for the persistent severe fog and haze event over eastern China in January 2013. *SCIENCE CHINA Earth Sciences*, **57**, 26-35, doi:10.1007/s11430-013-4774-3, 2014.

Zhang, Y. J., Zhang, P. Q., Wang, J., et al.: Climatic Characteristics of Persistent Haze Events over Jingjinji During 1981-2013. *Meteorological Monthly*, **41**, 311-318, doi:10.7519/j.issn.1000-0526.2015.03.006, 2015.

Zhong, Z., Yuan, H. H., Li, J., et al.: Characteristics of meso-scale perturbation and momentum transportation associated with an intensification process of upper-level jet. *Journal of the Meteorological Sciences*, **30**, 639-645, 2010.

Figure and table Captions:

Table 1. The timetable of 14 severe haze and 12 non-haze episodes. Note that the severe haze episodes are marked by gray shading. The unit of the $PM_{2.5}$ concentration is $\mu g \cdot m^{-3}$. The start time and end time are all in Beijing local time.

Table 2. The SPCCs between the mean $PM_{2.5}$ concentration over the BTH region and key meteorological indexes. All the SPCCs exceeded the 99% confidence level. The visibility, surface wind speed and surface relative humidity (RH) were based on the observation data and calculated as the mean over the BTH region. The temperature inversion potential (TIP, defined as T_{850}-T_{1000}) anomalies were calculated as the mean over the BTH region and with respect to the 1979-2010 climatology. The planetary boundary layer height (PBLH) anomalies were calculated as the mean over the BTH region and with respect to the 1979-2010 climatology. The synoptic process correlation coefficients (SPCCs) were calculated basing on the SPM data, which were rebuilt by averaging the mean $PM_{2.5}$ concentration, all the meteorological data and the AANA indexes during each severe haze (14), non-haze (12) and non-severe haze (24) process. The sample size was 50.

Table 3. The SPCCs between $AANAI_{Z500}$ ($AANAI_{V850}$, $AANAI_{\omega500}$) and regional meteorological indexes. "*" represents that the SPCC exceeded the 95% confidence level, and "**" represents that the SPCC exceeded the 99% confidence level. The synoptic process correlation coefficients (SPCCs) were calculated basing on the SPM data, which were rebuilt by averaging all the meteorological data and the AANA indexes during each severe haze (14), non-haze (12) and non-severe haze (24) process. The sample size was 50.

Table 4. The SPCCs between the mean $PM_{2.5}$ concentration over the BTH region and key indexes in December 2014, December 2015, December 2016 and December 2017. "*" represents that the SPCC exceeded the 95% confidence level, and "**" represents that the SPCC exceeded the 99% confidence level. The synoptic process correlation coefficients (SPCCs) were calculated basing on the SPM data, which were rebuilt by averaging the mean $PM_{2.5}$ concentration, all the meteorological data and the AANA indexes during each severe haze, non-haze and non-severe haze process. The sample sizes in 2014, 2015, 2016 and 2017 were 18, 14, 18 and 15, respectively. Note that the PBLH from the FNL data is available only after 2015.

Table 5. The SPCCs between $AANAI_{Z500}$ ($AANAI_{V850}$, $AANAI_{\omega500}$) and regional meteorological indexes in December 2014, December 2015, December 2016 and December 2017. "*" represents that the SPCC exceeded the 95% confidence level, and "**" represents that the SPCC exceeded the 99% confidence level. The synoptic process correlation coefficients (SPCCs) were calculated basing on the SPM data, which were rebuilt by averaging all the meteorological data and the AANA indexes during

each severe haze, non-haze and non-severe haze process. The sample sizes in 2014, 2015, 2016 and 2017 were 18, 14, 18 and 15, respectively. Note that the PBLH from the FNL data is available only after 2015.

Figure 1. The six-hour variation of mean $PM_{2.5}$ concentration over the BTH region (units: $\mu g \cdot m^{-3}$) in December 2014, December 2015 and December 2016. The time series (concentrations) corresponding to the red/blue lines represent the occurrence time (threshold values) of severe haze/non-haze episodes, respectively.

Figure 2. Composite distribution of the atmospheric circulation anomalies on severe haze/non-haze episodes. The anomalies here were calculated with respect to the 1979-2010 climatology. The green (white) box indicates the BTH region (area covered by $AANAI_{Z500}$). (a) Z_{500} (shading, units: $m^2 \cdot s^{-2}$) and U_{200} (contour, units: $m \cdot s^{-1}$) on severe haze episodes; the white dots indicate that the Z_{500} anomalies exceeded the 95% confidence level. (b) SLP (shading, units: hPa) and SAT (contour, units: K) on severe haze episodes; the white dots indicate that the SLP anomalies exceeded the 95% confidence level. (c) Z_{500} (shading, units: $m^2 \cdot s^{-2}$) and U_{200} (contour, units: $m \cdot s^{-1}$) on non-haze episodes; the white dots indicate that the Z_{500} anomalies exceeded the 95% confidence level. (d) SLP (shading, units: hPa) and SAT (contour, units: K) on non-haze episodes; the white dots indicate that the SLP anomalies exceeded the 95% confidence level.

Figure 3. Composite distribution of local atmospheric circulation anomalies on severe haze/non-haze episodes. The anomalies here were calculated with respect to the 1979-2010 climatology. The green (black) box indicates the BTH region (area covered by $AANAI_{V850}$). (a) $\boldsymbol{V}_{850}$ (arrow, units: $m \cdot s^{-1}$), PBLH (contour, units: m) and temperature inversion potential (T_{850}-T_{1000}, shading, units: K) on severe haze episodes; the bold black contours plotted represent the PBLH anomaly was lower than -200m; the white dots indicate that the temperature inversion potential anomalies exceeded the 95% confidence level. (b) Surface wind (arrow, units: $m \cdot s^{-1}$) and surface RH (shading, units: %) on severe haze episodes; the white dots indicate that the surface RH anomalies exceeded the 95% confidence level. (c) $\boldsymbol{V}_{850}$ (arrow, units: $m \cdot s^{-1}$), PBLH (contour, units: m) and temperature inversion potential (T_{850}-T_{1000}, shading, units: K) on non-haze episodes; the bold black contours plotted represent the PBLH anomaly was greater than 200m; the white dots indicate that the temperature inversion potential anomalies exceeded the 95% confidence level. (d) Surface wind (arrow, units: $m \cdot s^{-1}$) and surface RH (shading, units: %) on non-haze episodes; the white dots indicate that the surface RH anomalies exceeded the 95% confidence level.

Figure 4. The six-hour variation of $PM_{2.5}$ concentration, surface wind speed, surface RH, and TIP in December 2014, December 2015 and December 2016. The data were processed by min-max normalization. The time series corresponding to red/blue shading represent the occurrence time of severe haze/non-haze episodes. Note that every red/blue shading represents a synoptic process of severe haze/non-haze. The processes between severe haze and non-haze were defined as non-severe haze processes to represent the normal situation. The synoptic process mean (SPM) data were rebuilt by averaging the $PM_{2.5}$ concentration and all the meteorological data during each process.

Figure 5. The six-hour variation of $PM_{2.5}$ concentration, $AANAI_{Z500}$, $AANAI_{V850}$, and $AANAI_{\omega 500}$ in December 2014, December 2015 and December 2016. The time series corresponding to red/blue shading represent the occurrence time of severe haze/non-haze episodes. Note that every red/blue shading represents a synoptic process of severe haze/non-haze. The processes between severe haze and non-haze were defined as non-severe haze processes to represent the normal situation. The synoptic process mean (SPM) data were rebuilt by averaging the mean $PM_{2.5}$ concentration and all the AANA indexes during each process.

Figure 6. Structure of the AANA in the mid-levels: Z_{500} (contour, units: $m^2 \cdot s^{-2}$) and $\boldsymbol{\omega}_{500}$ (shading, units: $Pa \cdot s^{-1}$). The anomalies here were calculated with respect to the 1979-2010 climatology. The green (gray) box indicates the BTH region (area covered by $AANAI_{\omega 500}$). (a) severe haze episodes, (b) non-haze episodes. The white dots indicate that the $\boldsymbol{\omega}_{500}$ anomalies exceeded the 95% confidence level.

Figure 7. The differences of temperature changes (units: $10^{-5} K \cdot s^{-1}$) between severe haze and non-haze events over the BTH region. “Day+0” refers to the first day of severe haze and non-haze events. “Day-1” refers to one day before the first day of severe haze and non-haze events. Day+1 refers to one day after the first day of severe haze and non-haze events. The black

line represents the local temperature changes (i.e., $\frac{\partial T}{\partial t}$). The red line represents the horizontal temperature advection (i.e., $-\boldsymbol{V} \cdot \nabla T$). The blue line represents the combined effect of adiabatic compression and vertical advection (i.e., $(\frac{\kappa T}{P} - \frac{\partial T}{\partial P})\omega$, $\kappa = R/C_p = 0.286$; Wallace and Hobbs, 2006). The purple line represents the effect of diabatic heating process (i.e., $\frac{J}{C_p}$, J represents diabatic heating rate; this term was obtained through residual calculation) "ⓧ" indicates that the differences of the term between severe haze and non-haze exceeded the 95% confidence level.

Figure 8. Vertical circulation on severe haze/non-haze episodes (composite anomalies): (a) meridional circulation averaged over the AANA (115°-125°E) on severe haze episodes (vertical velocity, shading, units: $\mathrm{Pa \cdot s^{-1}}$; the vectors represent the vertical and meridional components); the white dots indicate that the vertical velocity anomalies exceeded the 95% confidence level. (b) zonal-vertical circulation averaged over the AANA (30°-40°N) on severe haze episodes (vertical velocity, shading, units: $\mathrm{Pa \cdot s^{-1}}$; the vectors represent the vertical and zonal components) and RH anomalies (contour, units: %); the white dots indicate that the RH anomalies exceeded the 95% confidence level. (c) meridional circulation averaged over the AANA (115°-125°E) on non-haze episodes (vertical velocity, shading, units: $\mathrm{Pa \cdot s^{-1}}$; the vectors represent the vertical and meridional components); the white dots indicate that the vertical velocity anomalies exceeded the 95% confidence level. (d) zonal-vertical circulation averaged over the AANA (30°-40°N) on non-haze episodes (vertical velocity, shading, units: $\mathrm{Pa \cdot s^{-1}}$; the vectors represent the vertical and zonal components) and RH (contour, units: %); the white dots indicate that the RH anomalies exceeded the 95% confidence level. The anomalies here were calculated with respect to the 1979-2010 climatology. To make the horizontal velocity and the vertical velocity in the same order, the vertical velocity (omega) here was magnified 100 times.

Figure 9. Vertical circulation on severe haze/non-haze episodes (composite synoptic processes): (a) meridional circulation averaged over the BTH region (114°-120°E) on severe haze episodes (vertical velocity, shading, units: $\mathrm{Pa \cdot s^{-1}}$; the vectors represent the vertical and meridional components); the white dots indicate that vertical velocity exceeded the 95% confidence level. (b) zonal-vertical circulation (36°-42°N mean) on severe haze episodes (the vectors represent the vertical and zonal components) and the vertical transport of westerly momentum (shading, units: $10^{-5}\mathrm{m \cdot s^{-2}}$); the white dots indicate that the vertical transport of westerly momentum exceeded the 95% confidence level. (c) meridional circulation averaged over the BTH region (114°-120°E) on non-haze episodes (vertical velocity, shading, units: $\mathrm{Pa \cdot s^{-1}}$; the vectors represent the vertical and meridional components); the white dots indicate that vertical velocity exceeded the 95% confidence level. (d) zonal-vertical circulation (36°-42°N mean) on non-haze episodes (the vectors represent the vertical and zonal components) and the vertical transport of westerly momentum (shading, units: $10^{-5}\mathrm{m \cdot s^{-2}}$); the white dots indicate that the vertical transport of westerly momentum exceeded the 95% confidence level. To make the horizontal velocity and the vertical velocity in the same order, the vertical velocity (omega) here was magnified 100 times.

Figure 10. Evolution of the AANA on severe haze episodes (a-g) and non-haze episodes (h-n): Z_{500} (contour, units: $m^2 \cdot \mathrm{s^{-2}}$), $\boldsymbol{V}_{850}$ (arrow, units: $\mathrm{m \cdot s^{-1}}$) and $\boldsymbol{\omega}_{500}$ (shading, units: $\mathrm{Pa \cdot s^{-1}}$). The anomalies here were calculated with respect to the 1979-2010 climatology. Severe haze/non-haze day+0 refers to the first day of severe haze/non-haze. Severe haze (non-haze) day-3, severe haze (non-haze) day-2, and severe haze (non-haze) day-1 refer to three, two, and one day(s) before the first day of severe haze (non-haze), respectively. Severe haze (non-haze) day+1, severe haze (non-haze) day+2, and severe haze (non-haze) day+3 refer to one, two, and three day(s) after the first day of severe haze (non-haze), respectively. The green box indicates the BTH region. The white, black and gray boxes indicate the area covered by AANAI_{Z500} $\mathrm{AANAI}_{\boldsymbol{V}850}$ and $\mathrm{AANAI}_{\boldsymbol{\omega}500}$, respectively.

Figure 11. Structure of the AANA on (a) severe haze episodes and (b) non-haze episodes in December 2017: Z_{500} (contour, units: $m^2 \cdot \mathrm{s^{-2}}$), $\boldsymbol{V}_{850}$ (arrow, units: $\mathrm{m \cdot s^{-1}}$) and $\boldsymbol{\omega}_{500}$ (shading, units: $\mathrm{Pa \cdot s^{-1}}$). The anomalies here were calculated with respect to the 1979-2010 climatology. The green box indicates the BTH region. The white, black and gray boxes indicate the area covered by AANAI_{Z500} $\mathrm{AANAI}_{\boldsymbol{V}850}$ and $\mathrm{AANAI}_{\boldsymbol{\omega}500}$, respectively.

Table 1. The timetable of 14 severe haze and 12 non-haze episodes. Note that the severe haze episodes are marked by gray shading. The unit of the $PM_{2.5}$ concentration is $\mu g \cdot m^{-3}$. The start time and end time are all in Beijing local time.

Year	Start time	End time	Mean concentration	Start time	End time	Mean concentration
2014	1st 08:00	5th 14:00	36.69	18th 20:00	19th 08:00	156.22
	9th 08:00	10th 08:00	169.70	19th 20:00	21st 20:00	31.62
	10th 20:00	13th 14:00	42.52	23rd 20:00	24th 02:00	170.25
	14th 20:00	15th 08:00	163.05	27th 02:00	28th 14:00	210.76
	15th 14:00	17th 14:00	33.32	31st 02:00	31st 20:00	28.21
2015	1st 08:00	2nd 02:00	200.11	20th 20:00	26th 08:00	221.44
	2nd 14:00	4th 20:00	26.37	27th 02:00	27th 20:00	32.55
	7th 20:00	10th 08:00	219.65	29th 02:00	30th 08:00	193.29
	15th 08:00	17th 14:00	23.74			
2016	2nd 20:00	5th 02:00	192.60	16th 20:00	22nd 02:00	227.48
	5th 14:00	5th 20:00	44.17	23rd 08:00	23rd 14:00	39.75
	8th 20:00	9th 20:00	37.24	25th 20:00	26th 02:00	162.07
	11th 20:00	12th 20:00	175.91	30th 14:00	31st 20:00	209.76
	13th14:00	14th 14:00	40.82			

Table 2. The SPCCs between the mean $PM_{2.5}$ concentration over the BTH region and key meteorological indexes. All the SPCCs exceeded the 99% confidence level. The visibility, surface wind speed and surface relative humidity (RH) were based on the observation data and calculated as the mean over the BTH region. The temperature inversion potential (TIP, defined as T_{850}-T_{1000}) anomalies were calculated as the mean over the BTH region and with respect to the 1979-2010 climatology. The planetary boundary layer height (PBLH) anomalies were calculated as the mean over the BTH region and with respect to the 1979-2010 climatology. The synoptic process correlation coefficients (SPCCs) were calculated basing on the SPM data, which were rebuilt by averaging the mean $PM_{2.5}$ concentration, all the meteorological data and the AANA indexes during each severe haze (14), non-haze (12) and non-severe haze (24) process. The sample size was 50.

Index	AANA I_{Z500}	AANA I_{V850}	AANA $I_{\omega 500}$	Visibility	Surface wind speed	Surface RH	TIP anomalies	ERA PBLH anomalies
SPCC	0.64	-0.64	-0.70	-0.83	-0.42	0.72	0.56	-0.60

Table 3. The SPCCs between $AANAI_{Z500}$ ($AANAI_{V850}$, $AANAI_{\omega 500}$) and regional meteorological indexes. "*" represents that the SPCC exceeded the 95% confidence level, and "**" represents that the SPCC exceeded the 99% confidence level. The synoptic process correlation coefficients (SPCCs) were calculated basing on the SPM data, which were rebuilt by averaging all the meteorological data and the AANA indexes during each severe haze (14), non-haze (12) and non-severe haze (24) process. The sample size was 50.

SPCC	Visibility	Surface wind speed	Surface RH	TIP anomalies	ERA PBLH anomalies
$AANAI_{Z500}$	-0.71^{**}	-0.38^{**}	0.73^{**}	0.58^{**}	-0.50^{**}
$AANAI_{V850}$	0.59^{**}	0.25	-0.56^{**}	-0.41^{**}	0.40^{**}
$AANAI_{\omega 500}$	0.51^{**}	0.11	-0.50^{**}	-0.30^{*}	0.22

Table 4. The SPCCs between the mean $PM_{2.5}$ concentration over the BTH region and key indexes in December 2014, December 2015, December 2016 and December 2017. "*" represents that the SPCC exceeded the 95% confidence level, and "**" represents that the SPCC exceeded the 99% confidence level. The synoptic process correlation coefficients (SPCCs) were calculated basing on the SPM data, which were rebuilt by averaging the mean $PM_{2.5}$ concentration, all the meteorological data and the AANA indexes during each severe haze, non-haze and non-severe haze process. The sample sizes in 2014, 2015, 2016 and 2017 were 18, 14, 18 and 15, respectively. Note that the PBLH from the FNL data is available only after 2015.

SPCC	AANA I_{500}	AANA I_{850}	AANA $I_{\omega 500}$	Visibility	Surface wind speed	Surface RH	TIP anomalies	ERA PBLH anomalies	FNL PBLH
2014	0.81**	-0.72**	-0.77**	-0.76**	-0.36	0.75**	0.69**	-0.65**	
2015	0.53	-0.61*	-0.66*	-0.94**	-0.53*	0.92**	0.37	-0.63*	-0.72**
2016	0.79**	-0.62**	-0.70**	-0.9**	-0.52*	0.87**	0.80**	-0.63**	-0.70**
2017	0.73**	-0.33	-0.58*	-0.89**	-0.68**	-0.86**	0.68**	-0.73**	-0.68**

Table 5. The SPCCs between $AANAI_{Z500}$ ($AANAI_{V850}$, $AANAI_{\omega 500}$) and regional meteorological indexes in December 2014, December 2015, December 2016 and December 2017. "*" represents that the SPCC exceeded the 95% confidence level, and "**" represents that the SPCC exceeded the 99% confidence level. The synoptic process correlation coefficients (SPCCs) were calculated basing on the SPM data, which were rebuilt by averaging all the meteorological data and the AANA indexes during each severe haze, non-haze and non-severe haze process. The sample sizes in 2014, 2015, 2016 and 2017 were 18, 14, 18 and 15, respectively. Note that the PBLH from the FNL data is available only after 2015.

Year	SPCC	Visibility	Surface wind speed	Surface RH	TIP anomalies	ERA PBLH anomalies	FNL PBLH
2014	$AANAI_{Z500}$	-0.64**	-0.10	0.57*	0.62**	-0.39	
	$AANAI_{V850}$	0.35	-0.09	-0.38	-0.27	0.22	
	$AANAI_{\omega 500}$	0.46	-0.01	-0.45	-0.45	0.27	
2015	$AANAI_{Z500}$	-0.66*	-0.68**	0.64*	0.07	-0.46	-0.65*
	$AANAI_{V850}$	0.75**	0.74**	-0.70**	-0.22	0.64*	0.72**
	$AANAI_{\omega 500}$	0.67**	0.35	-0.79**	-0.24	0.28	0.46
2016	$AANAI_{Z500}$	-0.70**	-0.46	0.69**	0.67**	-0.53*	-0.56*
	$AANAI_{V850}$	0.69**	0.46	-0.60**	-0.56*	0.47	0.60**
	$AANAI_{\omega 500}$	0.64**	0.26	-0.80**	-0.45	0.20	0.55*
2017	$AANAI_{Z500}$	-0.74**	-0.57*	0.65**	0.72**	-0.66**	-0.59*
	$AANAI_{V850}$	0.17	0.03	0.01	0.16	0.12	0.05
	$AANAI_{\omega 500}$	0.48	0.40	-0.39	-0.41	0.62*	0.58*

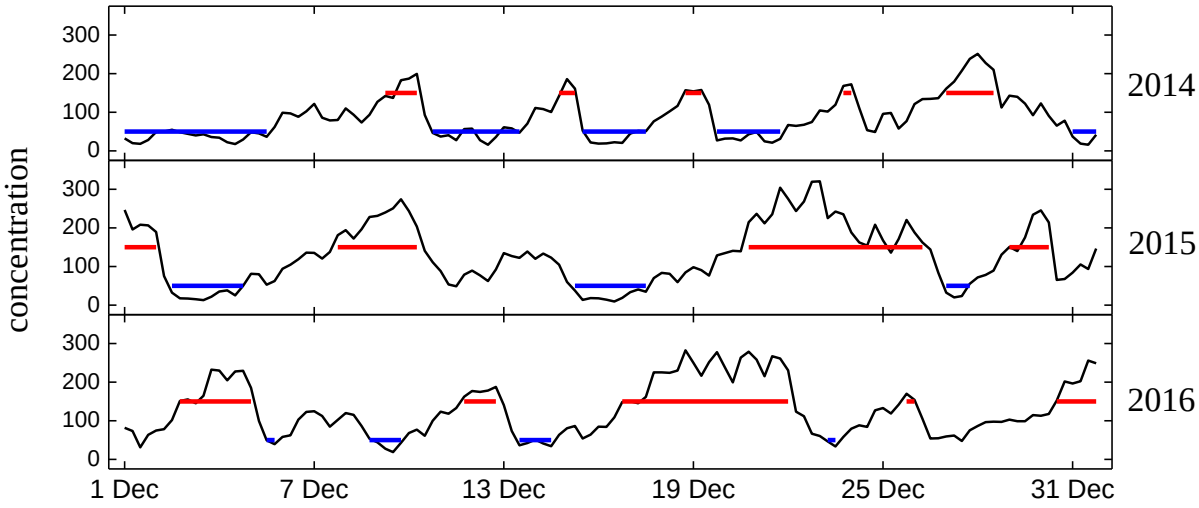

Figure 1. The six-hour variation of mean $PM_{2.5}$ concentration over the BTH region (units: $\mu g \cdot m^{-3}$) in December 2014, December 2015 and December 2016. The time series (concentrations) corresponding to the red/blue lines represent the occurrence time (threshold values) of severe haze/non-haze episodes, respectively.

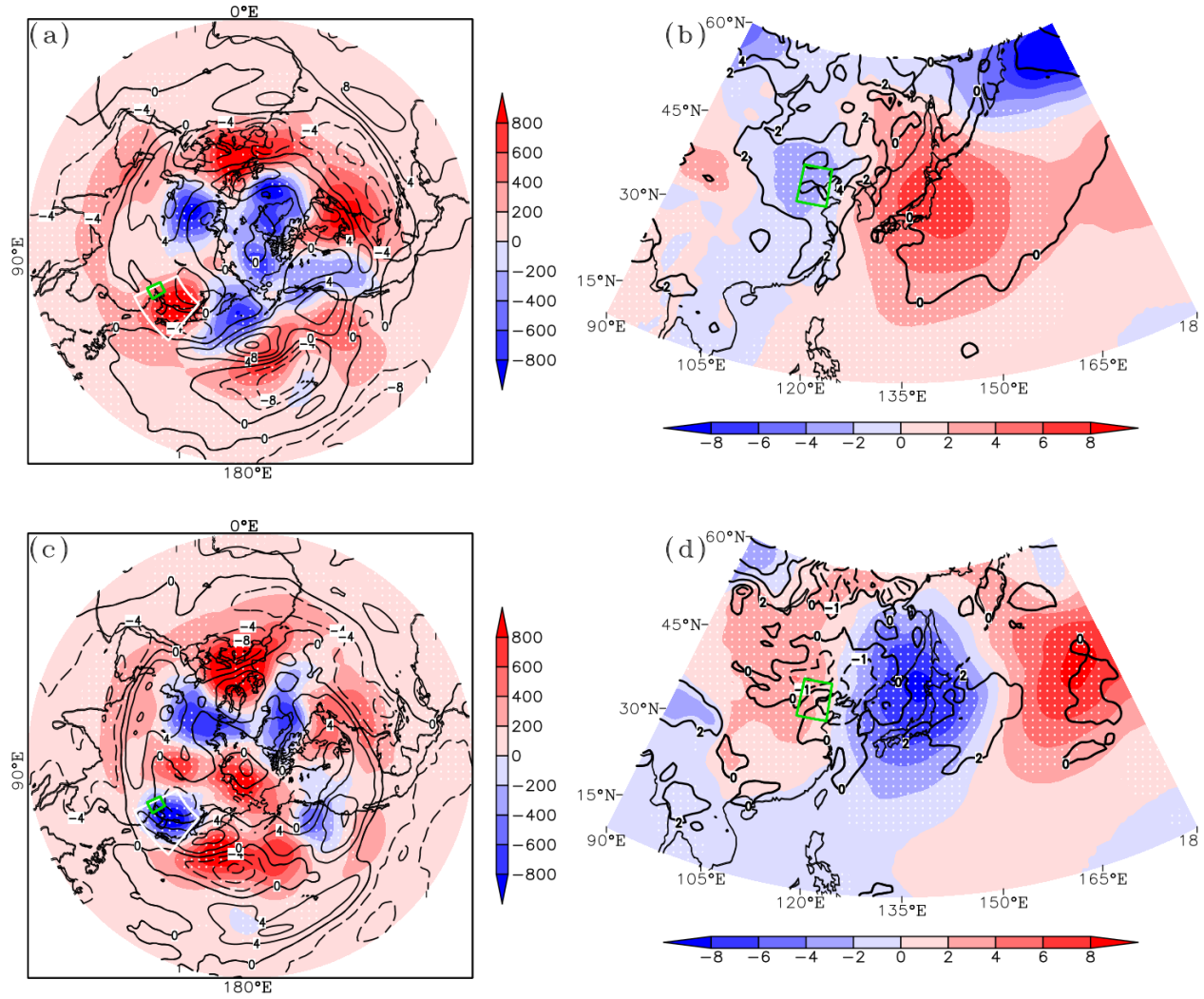

Figure 2. Composite distribution of the atmospheric circulation anomalies on severe haze/non-haze episodes. The anomalies here were calculated with respect to the 1979-2010 climatology. The green (white) box indicates the BTH region (area covered by $AANAI_{Z500}$). (a) Z_{500} (shading, units: $m^2 \cdot s^{-2}$) and U_{200} (contour, units: $m \cdot s^{-1}$) on severe haze episodes; the white dots indicate that the Z_{500} anomalies exceeded the 95% confidence level. (b) SLP (shading, units: hPa) and SAT (contour, units: K) on severe haze episodes; the white dots indicate that the SLP anomalies exceeded the 95% confidence level. (c) Z_{500} (shading, units: $m^2 \cdot s^{-2}$) and U_{200} (contour, units: $m \cdot s^{-1}$) on non-haze episodes; the white dots indicate that the Z_{500} anomalies exceeded the 95% confidence level. (d) SLP (shading, units: hPa) and SAT (contour, units: K) on non-haze episodes; the white dots indicate that the SLP anomalies exceeded the 95% confidence level.

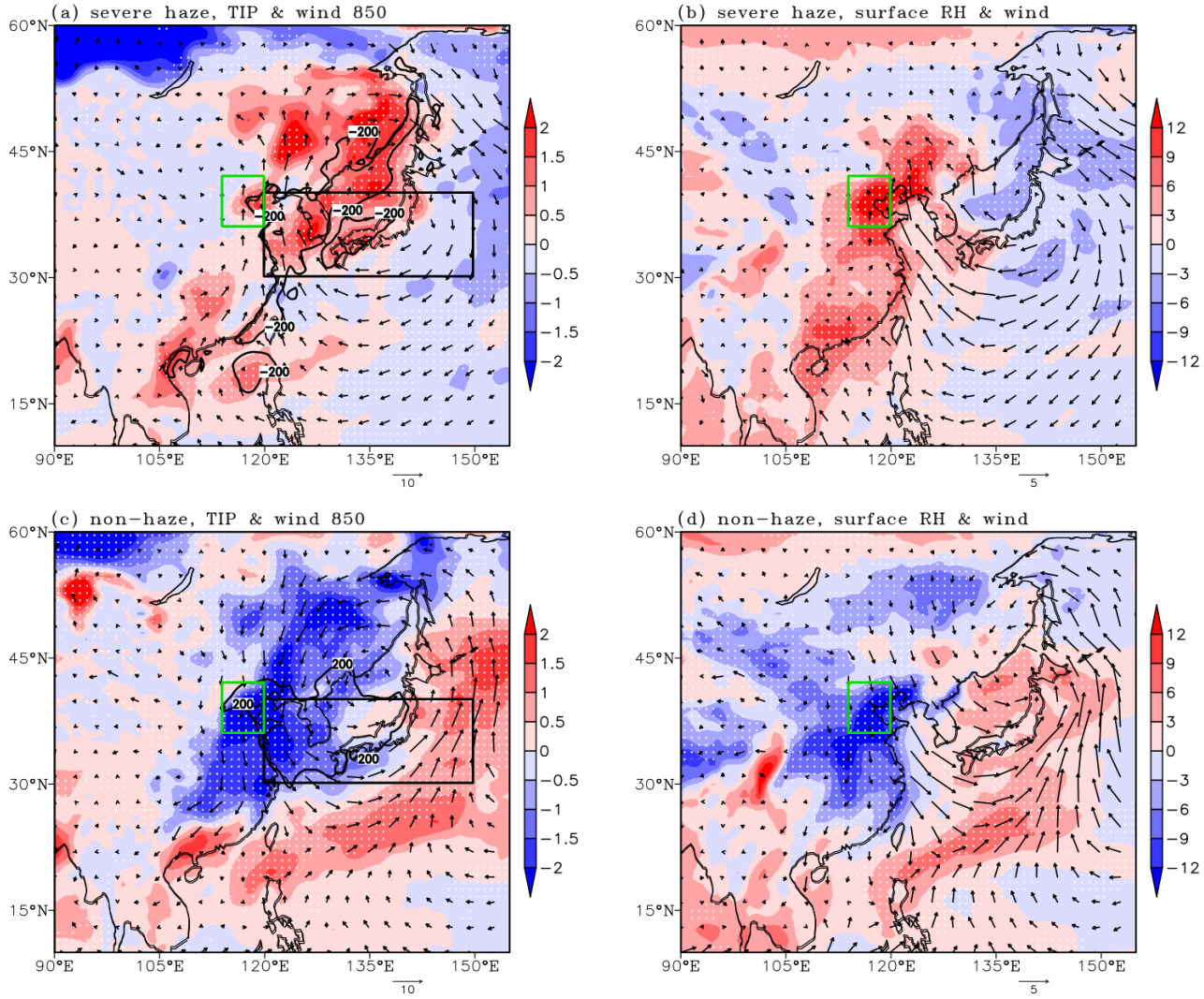

Figure 3. Composite distribution of local atmospheric circulation anomalies on severe haze/non-haze episodes. The anomalies here were calculated with respect to the 1979-2010 climatology. The green (black) box indicates the BTH region (area covered by $AANAI_{V850}$). (a) $\boldsymbol{V}_{850}$ (arrow, units: $m \cdot s^{-1}$), PBLH (contour, units: m) and temperature inversion potential (T_{850}-T_{1000}, shading, units: K) on severe haze episodes; the bold black contours plotted represent the PBLH anomaly was lower than -200m; the white dots indicate that the temperature inversion potential anomalies exceeded the 95% confidence level. (b) Surface wind (arrow, units: $m \cdot s^{-1}$) and surface RH (shading, units: %) on severe haze episodes; the white dots indicate that the surface RH anomalies exceeded the 95% confidence level. (c) $\boldsymbol{V}_{850}$ (arrow, units: $m \cdot s^{-1}$), PBLH (contour, units: m) and temperature inversion potential (T_{850}-T_{1000}, shading, units: K) on non-haze episodes; the bold black contours plotted represent the PBLH anomaly was greater than 200m; the white dots indicate that the temperature inversion potential anomalies exceeded the 95% confidence level. (d) Surface wind (arrow, units: $m \cdot s^{-1}$) and surface RH (shading, units: %) on non-haze episodes; the white dots indicate that the surface RH anomalies exceeded the 95% confidence level.

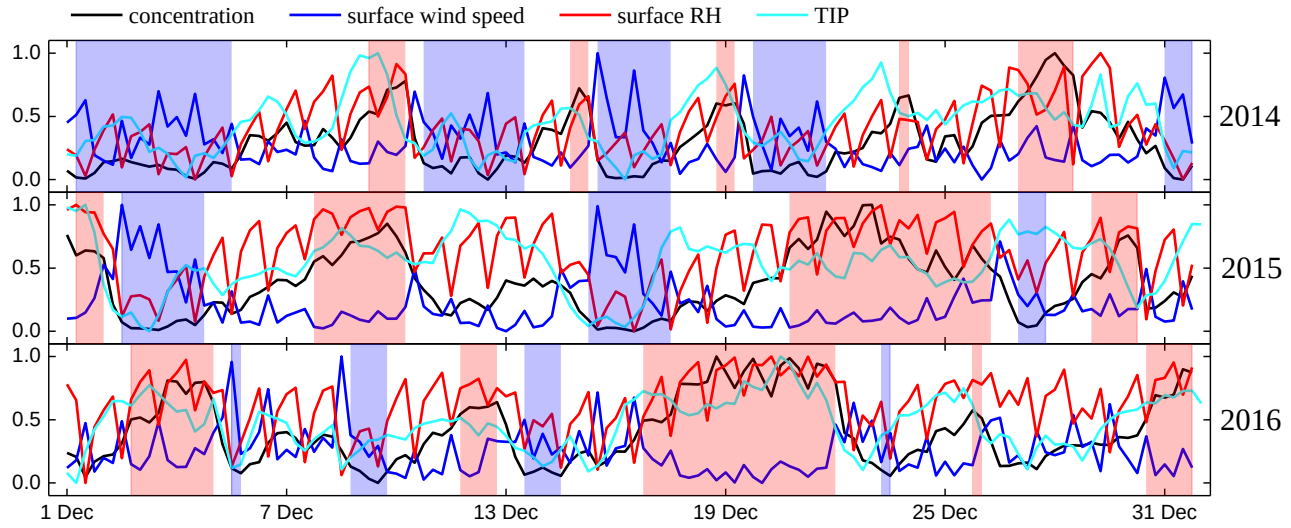

Figure 4. The six-hour variation of $PM_{2.5}$ concentration, surface wind speed, surface RH, and TIP in December 2014, December 2015 and December 2016. The data were processed by min-max normalization. The time series corresponding to red/blue shading represent the occurrence time of severe haze/non-haze episodes. Note that every red/blue shading represents a synoptic process of severe haze/non-haze. The processes between severe haze and non-haze were defined as non-severe haze processes to represent the normal situation. The synoptic process mean (SPM) data were rebuilt by averaging the $PM_{2.5}$ concentration and all the meteorological data during each process.

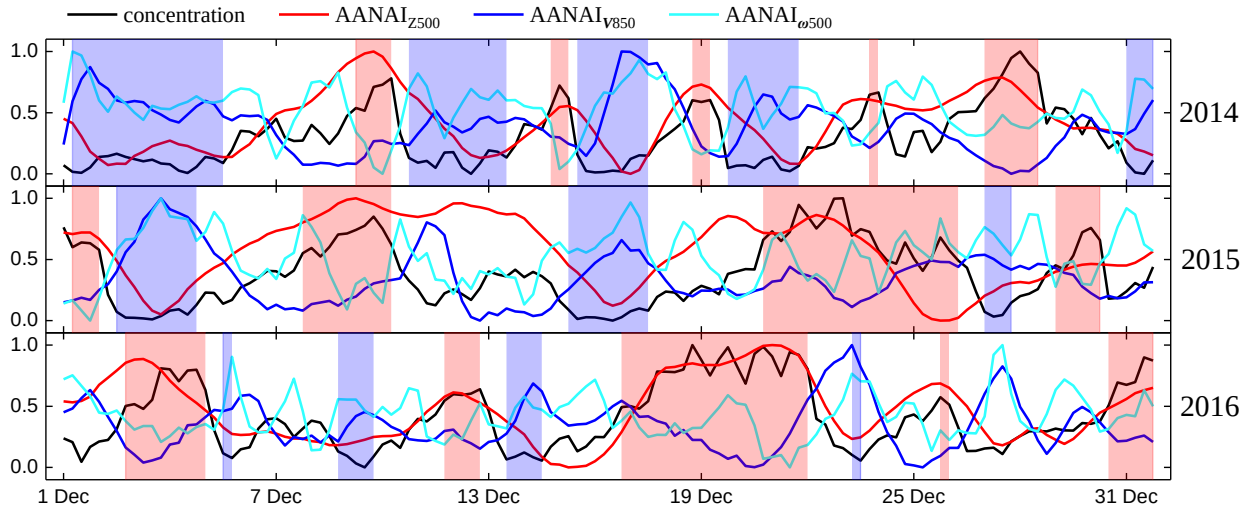

Figure 5. The six-hour variation of $PM_{2.5}$ concentration, $AANAI_{Z500}$, $AANAI_{V850}$, and $AANAI_{\omega 500}$ in December 2014, December 2015 and December 2016. The time series corresponding to red/blue shading represent the occurrence time of severe haze/non-haze episodes. Note that every red/blue shading represents a synoptic process of severe haze/non-haze. The processes between severe haze and non-haze were defined as non-severe haze processes to represent the normal situation. The synoptic process mean (SPM) data were rebuilt by averaging the mean $PM_{2.5}$ concentration and all the AANA indexes during each process.

590

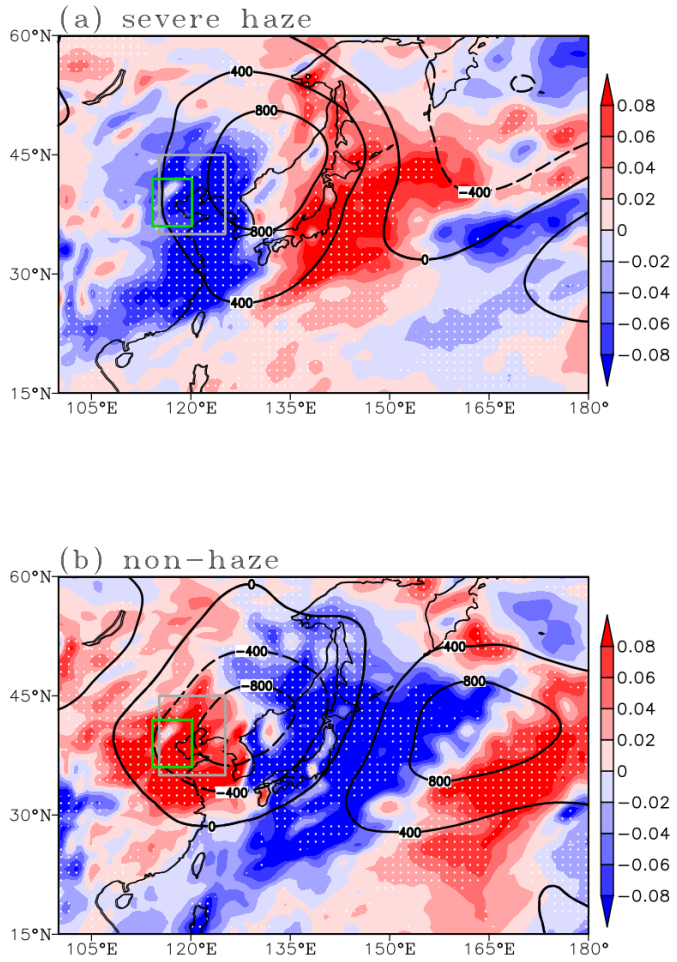

Figure 6. Structure of the AANA in the mid-levels: Z_{500} (contour, units: $m^2 \cdot s^{-2}$) and ω_{500} (shading, units: $Pa \cdot s^{-1}$). The anomalies here were calculated with respect to the 1979-2010 climatology. The green (gray) box indicates the BTH region (area covered by $AANAI_{\omega 500}$). (a) severe haze episodes, (b) non-haze episodes. The white dots indicate that the ω_{500} anomalies exceeded the 95% confidence level.

595

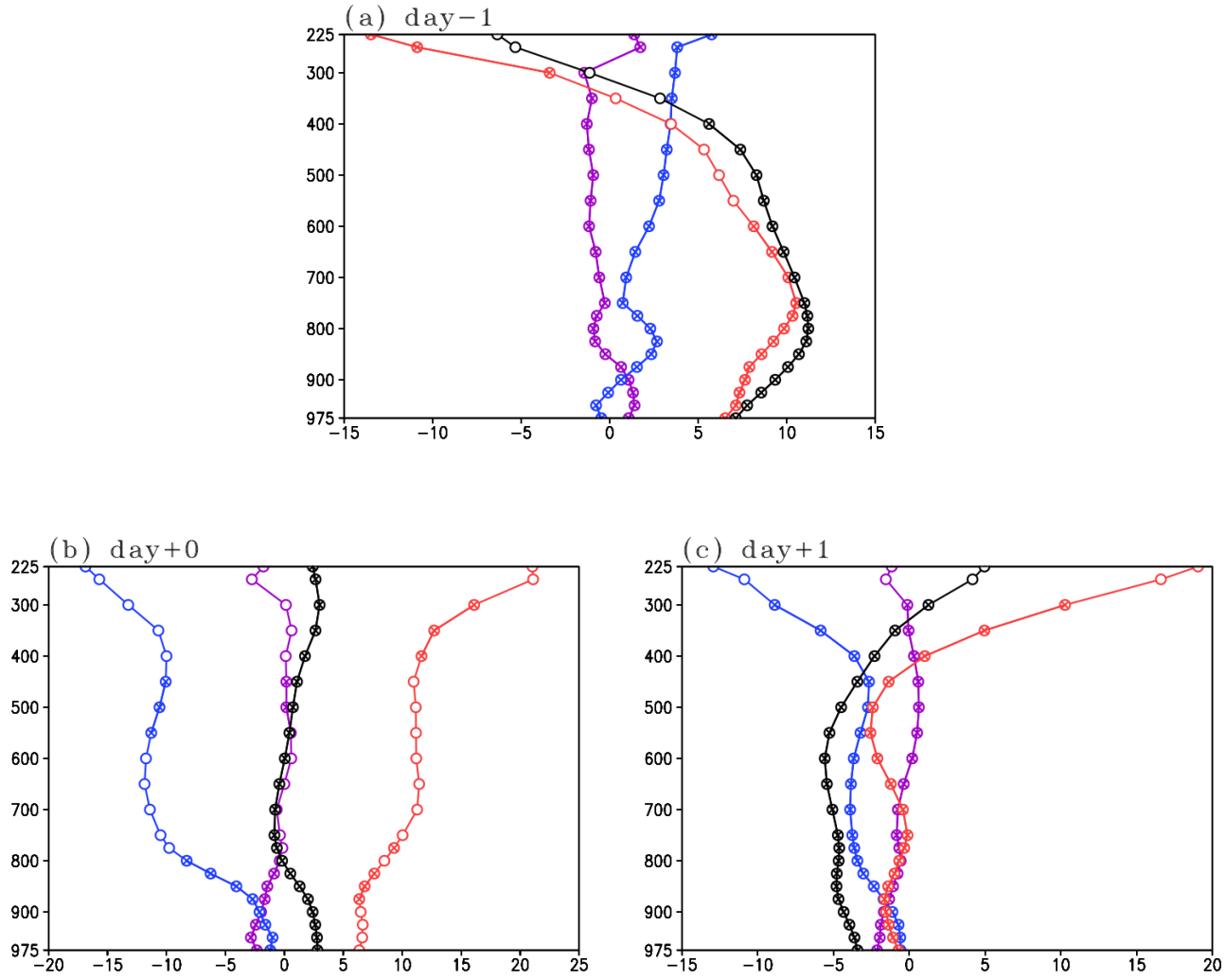

Figure 7. The differences of temperature changes (units: $10^{-5}\mathrm{K}\cdot\mathrm{s}^{-1}$) between severe haze and non-haze events over the BTH region. "Day+0" refers to the first day of severe haze and non-haze events. "Day-1" refers to one day before the first day of severe haze and non-haze events. Day+1 refers to one day after the first day of severe haze and non-haze events. The black line represents the local temperature changes (i.e., $\frac{\partial T}{\partial t}$). The red line represents the horizontal temperature advection (i.e., $-\boldsymbol{V}\cdot\nabla\mathrm{T}$). The blue line represents the combined effect of adiabatic compression and vertical advection (i.e., $(\frac{\kappa T}{P}-\frac{\partial T}{\partial P})\omega$, $\kappa = R/C_p = 0.286$; Wallace and Hobbs, 2006). The purple line represents the effect of diabatic heating process (i.e., $\frac{J}{C_p}$, J represents diabatic heating rate; this term was obtained through residual calculation) "ⓧ" indicates that the differences of the term between severe haze and non-haze exceeded the 95% confidence level.

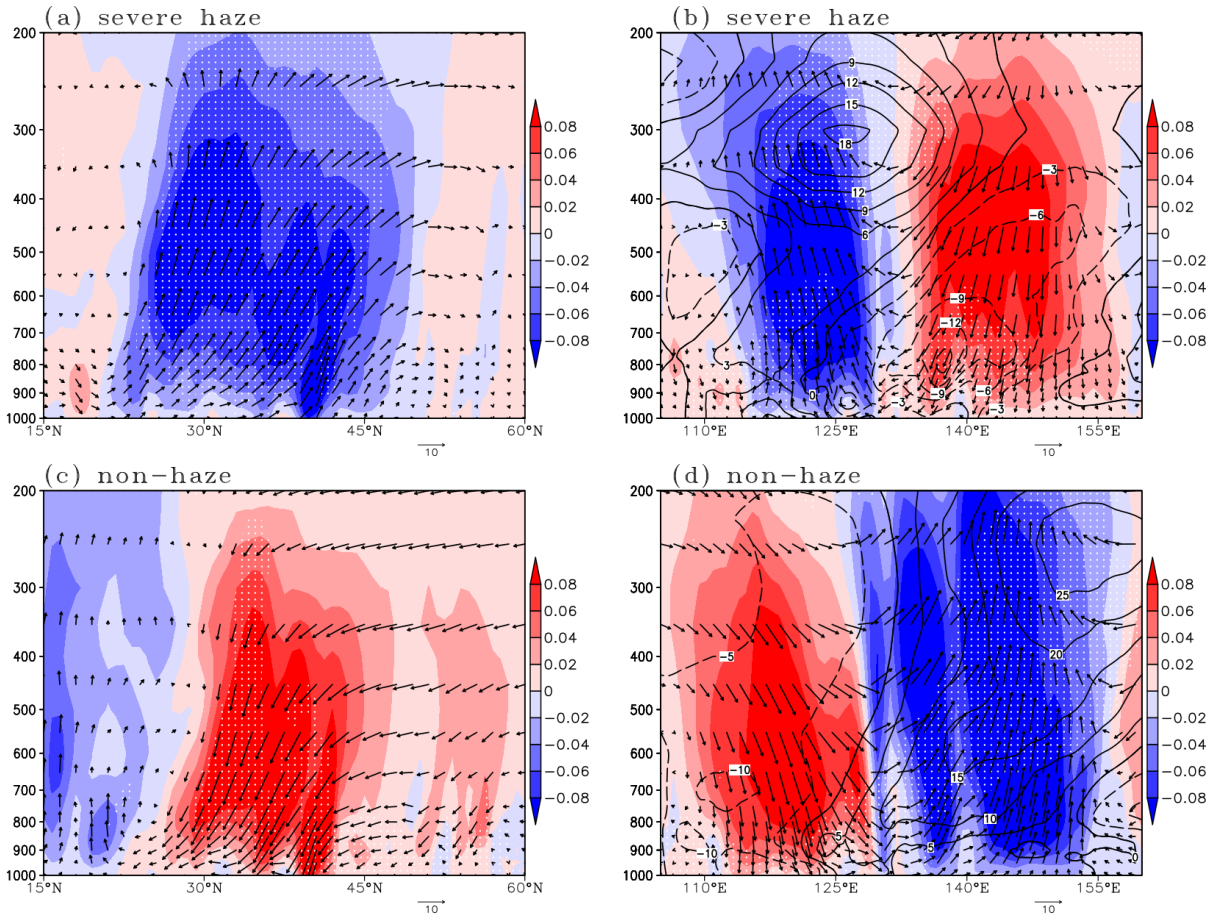

Figure 8. Vertical circulation on severe haze/non-haze episodes (composite anomalies): (a) meridional circulation averaged over the AANA (115°-125°E) on severe haze episodes (vertical velocity, shading, units: $Pa \cdot s^{-1}$; the vectors represent the vertical and meridional components); the white dots indicate that the vertical velocity anomalies exceeded the 95% confidence level. (b) zonal-vertical circulation averaged over the AANA (30°-40°N) on severe haze episodes (vertical velocity, shading, units: $Pa \cdot s^{-1}$; the vectors represent the vertical and zonal components) and RH anomalies (contour, units: %); the white dots indicate that the RH anomalies exceeded the 95% confidence level. (c) meridional circulation averaged over the AANA (115°-125°E) on non-haze episodes (vertical velocity, shading, units: $Pa \cdot s^{-1}$; the vectors represent the vertical and meridional components); the white dots indicate that the vertical velocity anomalies exceeded the 95% confidence level. (d) zonal-vertical circulation averaged over the AANA (30°-40°N) on non-haze episodes (vertical velocity, shading, units: $Pa \cdot s^{-1}$; the vectors represent the vertical and zonal components) and RH (contour, units: %); the white dots indicate that the RH anomalies exceeded the 95% confidence level. The anomalies here were calculated with respect to the 1979-2010 climatology. To make the horizontal velocity and the vertical velocity in the same order, the vertical velocity (omega) here was magnified 100 times.

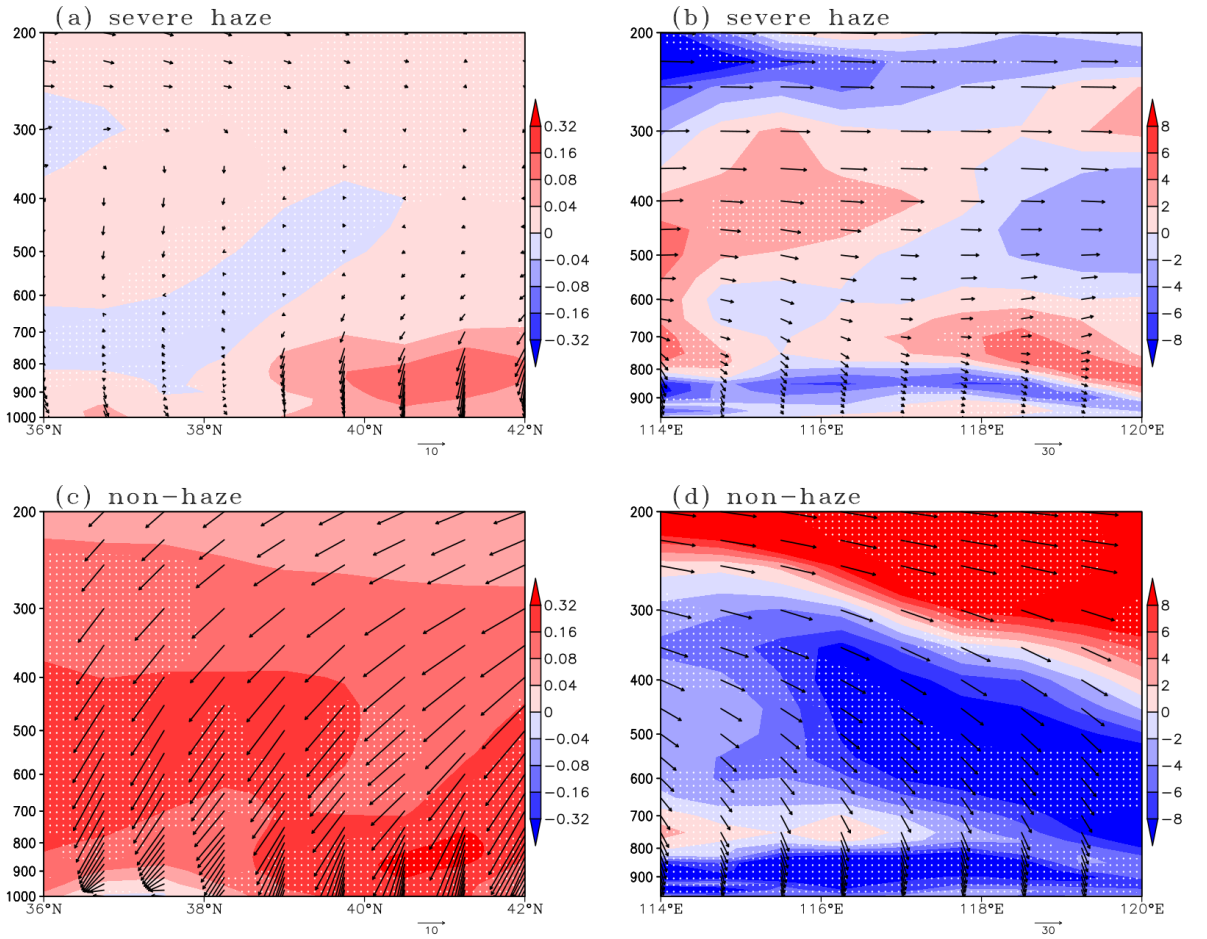

Figure 9. Vertical circulation on severe haze/non-haze episodes (composite synoptic processes): (a) meridional circulation averaged over the BTH region (114°-120°E) on severe haze episodes (vertical velocity, shading, units: $\mathrm{Pa \cdot s^{-1}}$; the vectors represent the vertical and meridional components); the white dots indicate that vertical velocity exceeded the 95% confidence level. (b) zonal-vertical circulation (36°-42°N mean) on severe haze episodes (the vectors represent the vertical and zonal components) and the vertical transport of westerly momentum (shading, units: $10^{-5}\mathrm{m \cdot s^{-2}}$); the white dots indicate that the vertical transport of westerly momentum exceeded the 95% confidence level. (c) meridional circulation averaged over the BTH region (114°-120°E) on non-haze episodes (vertical velocity, shading, units: $\mathrm{Pa \cdot s^{-1}}$; the vectors represent the vertical and meridional components); the white dots indicate that vertical velocity exceeded the 95% confidence level. (d) zonal-vertical circulation (36°-42°N mean) on non-haze episodes (the vectors represent the vertical and zonal components) and the vertical transport of westerly momentum (shading, units: $10^{-5}\mathrm{m \cdot s^{-2}}$); the white dots indicate that the vertical transport of westerly momentum exceeded the 95% confidence level. To make the horizontal velocity and the vertical velocity in the same order, the vertical velocity (omega) here was magnified 100 times.

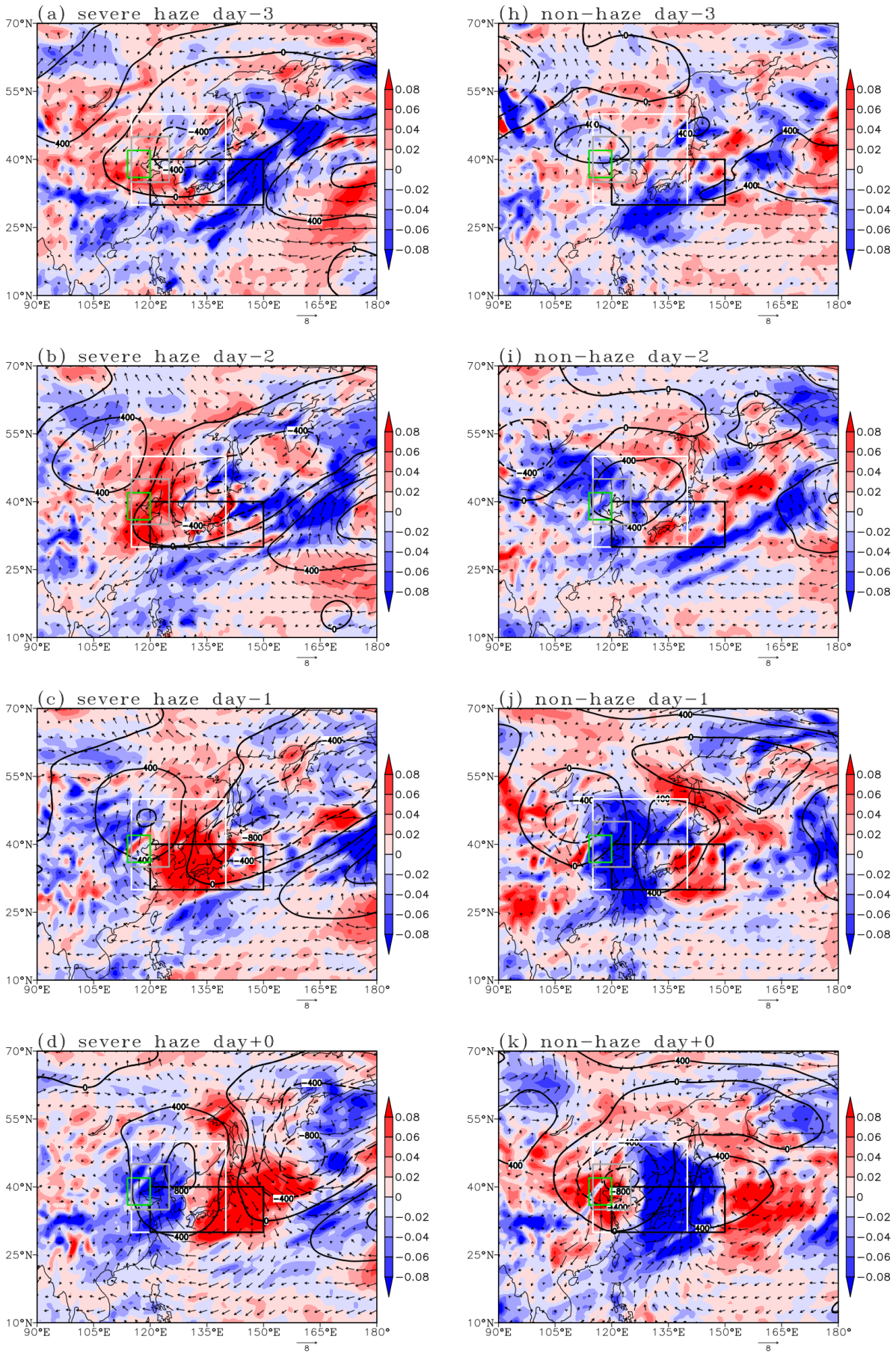
(a) severe haze day−3
(h) non−haze day−3
(b) severe haze day−2
(i) non−haze day−2
(c) severe haze day−1
(j) non−haze day−1
(d) severe haze day+0
(k) non−haze day+0
70°N
55°N
40°N
25°N
10°N
90°E
105°E
120°E
135°E
150°E
165°E
180°
0.08
0.06
0.04
0.02
0
−0.02
−0.04
−0.06
−0.08

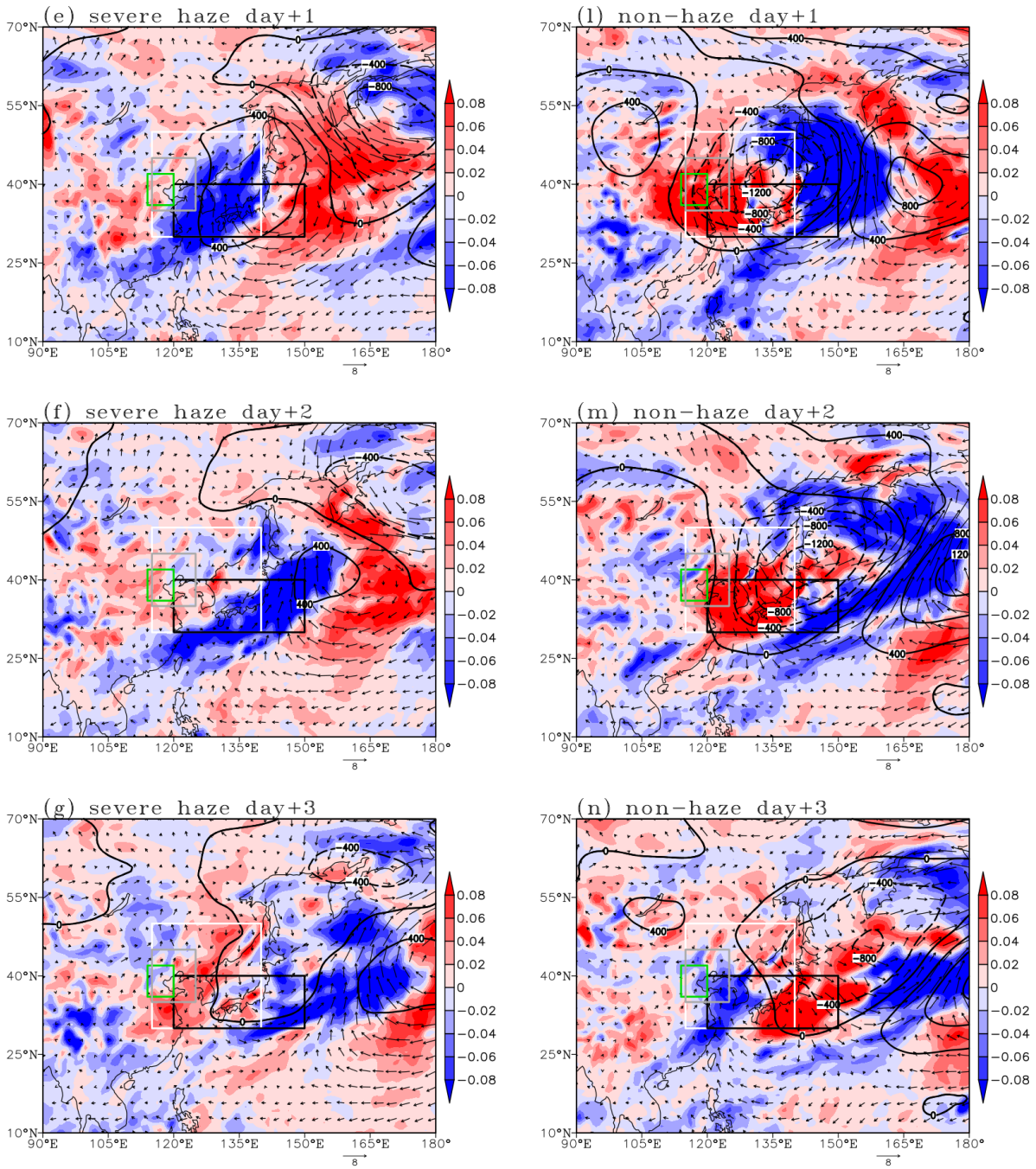

Figure 10. Evolution of the AANA on severe haze episodes (a-g) and non-haze episodes (h-n): Z_{500} (contour, units: $m^2 \cdot s^{-2}$), $\boldsymbol{V}_{850}$ (arrow, units: $m \cdot s^{-1}$) and $\boldsymbol{\omega}_{500}$ (shading, units: $Pa \cdot s^{-1}$). The anomalies here were calculated with respect to the 1979-2010 climatology. Severe haze/non-haze day+0 refers to the first day of severe haze/non-haze. Severe haze (non-haze) day-3, severe haze (non-haze) day-2, and severe haze (non-haze) day-1 refer to three, two, and one day(s) before the first day of severe haze (non-haze), respectively. Severe haze (non-haze) day+1, severe haze (non-haze) day+2, and severe haze (non-haze) day+3 refer to one, two, and three day(s) after the first day of severe haze (non-haze), respectively. The green box indicates the BTH region. The white, black and gray boxes indicate the area covered by $AANAI_{Z500}$ $AANAI_{\boldsymbol{V}850}$ and $AANAI_{\omega500}$, respectively.

600

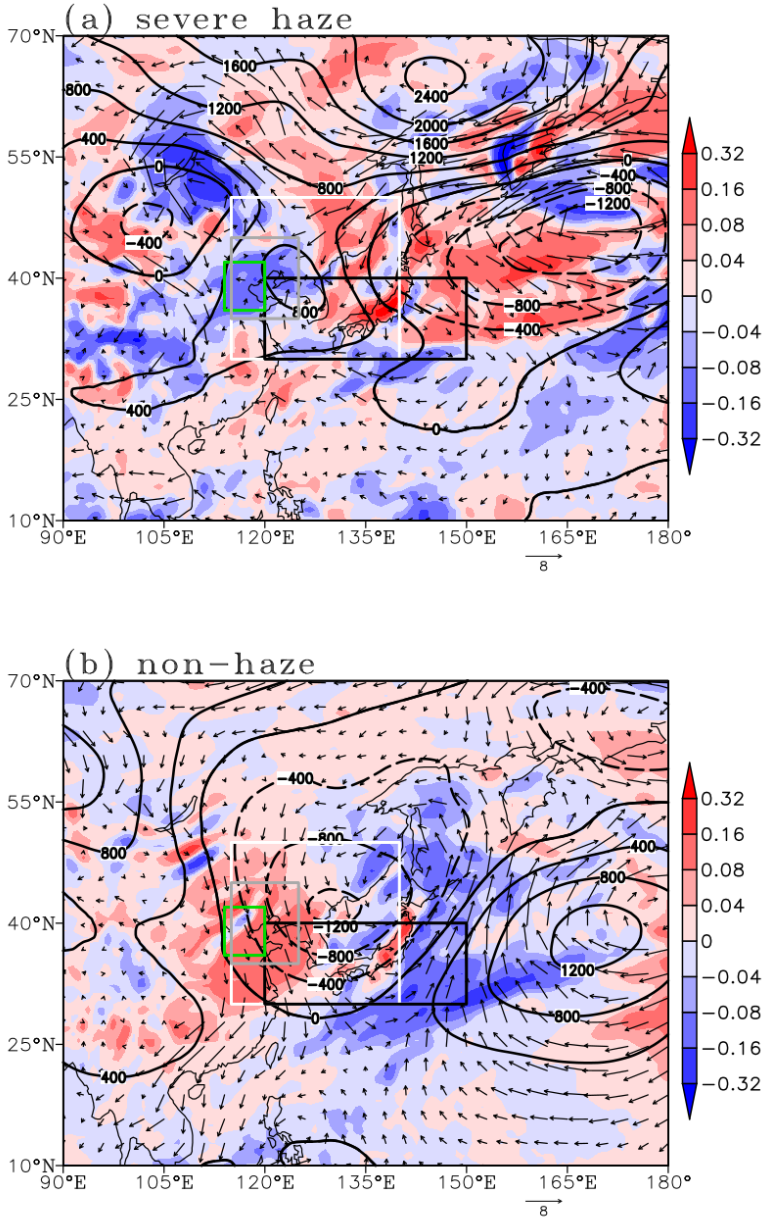

Figure 11. Structure of the AANA on (a) severe haze episodes and (b) non-haze episodes in December 2017: Z_{500} (contour, units: $m^2 \cdot s^{-2}$), $\boldsymbol{V}_{850}$ (arrow, units: $m \cdot s^{-1}$) and $\boldsymbol{\omega}_{500}$ (shading, units: $Pa \cdot s^{-1}$). The anomalies here were calculated with respect to the 1979-2010 climatology. The green box indicates the BTH region. The white, black and gray boxes indicate the area covered by $AANAI_{Z500}$ $AANAI_{V850}$ and $AANAI_{\omega 500}$, respectively.